LA-UR- 08-4998

Approved for public release;
distribution is unlimited.

Title:	Two Stochastic Mean-field Polycrystal Plasticity Methods
Author(s):	Michael Tonks-T3
Intended for:	International Journal of Plasticity

Los Alamos
NATIONAL LABORATORY
EST.1943

Form 836 (7/06)

Two Stochastic Mean-field Polycrystal Plasticity Methods

Michael R. Tonks [a,c] John F. Bingert [b] Curt A. Bronkhorst [a]

Eric N. Harstad [a] Daniel A. Tortorelli [c]

[a] *T-3, Los Alamos National Laboratory, Los Alamos, NM, 87545, USA*

[b] *MST-8, Los Alamos National Laboratory, Los Alamos, NM, 87545, USA*

[c] *Department of Mechanical Sciences and Engineering, University of Illinois at Urbana-Champaign, Urbana, IL 61801, USA*

Abstract

In this work, we develop two mean-field polycrystal plasticity models in which the $\mathbf{L}^c$ are approximated stochastically. Through comprehensive CPFEM analyses of an idealized tantalum polycrystal, we verify that the $\mathbf{L}^c$ tend to follow a normal distribution and surmise that this is due to the crystal interactions. We draw on these results to develop the STM and the stochastic no-constraints model (SNCM), which differ in the manner in which the crystal strain rates $\mathbf{D}^c$ are prescribed. Calibration and validation of the models are performed using data from tantalum compression experiments. Both models predict the compression textures more accurately than the FCM, and the SNCM predicts them more accurately than the STM. The STM is extremely computationally efficient, only slightly more expensive than the FCM, while the SNCM is three times more computationally expensive than the STM.

Key words: Polycrystal Plasticity, Stochastic Models, Texture Modeling

1 Introduction

Crystallographic textures, which evolve during forming processes, have large effects on the properties of the processed material. As such, the development of meaningful models for forming processes must consider texture evolution. This is a complicated task because texture modeling bridges multiple length scales. Indeed, material constitutive laws that calculate the macro-scale stress at a material point due to macro-scale deformation are not viable for polycrystalline materials whose behavior is attributed to the meso-scale crystal response.

To bridge the macro- and meso-scales, mean-field polycrystal plasticity models consider an aggregate of N crystals at each material point $\mathbf{x}$. For each crystal c in the material point aggregate the meso-scale model predicts the crystal Cauchy stress $\mathbf{T}^c$ given the crystal velocity gradient $\mathbf{L}^c$. The meso-scale $\mathbf{T}^c$ are subsequently averaged to obtain the macro-scale Cauchy stress $\mathbf{T}$ at this material point $\mathbf{x}$. However, in general, the macro-scale velocity gradient $\mathbf{L}$ is known, not the meso-scale $\mathbf{L}^c$. Consequently, a scheme is needed to map the macro-scale $\mathbf{L}$ to the meso-scale $\mathbf{L}^c$. Several models to this effect appear in the literature, the most common being the fully constrained model (FCM), based on the hypothesis in Taylor (1938) that the crystal deformations are equal to the macroscopic deformation, i.e. $\mathbf{L}^c = \mathbf{L}$. Although many applications of the FCM seem to validate its use (Harren and Asaro, 1989; Kalidindi et al., 1992), it does not maintain equilibrium in the aggregate; however it provides an upper bound on the work necessary to achieve the macro-scale $\mathbf{L}$ (Kocks et al., 1998). In contrast, the no-constraints model (NCM) assumes a homogeneous stress in the aggregate (Chastel and Dawson, 1994), i.e. $\mathbf{T}^c = \mathbf{T}$, but does not ensure compatibility. Hence, the NCM provides a lower bound on the work

(Kocks et al., 1998). Several alternative, less restrictive methods have been proposed. The visco-plastic self-consistent model (VPSC) describes each crystal as a viscoplastic inclusion embedded in a homogeneous effective medium with the average properties of the other crystals (Lebensohn and Tomé, 1993). Whereas, the grain-interaction (GIA) model enforces the relationship $\mathbf{L}^c = \mathbf{L}$ in an average sense over groups of eight crystals (Crumbach et al., 2001), thus accounting for local crystal interactions. Of course, the increased complexity of these models comes at the expense of additional computation.

In order to develop accurate means of obtaining $\mathbf{L}^c$, it is important to understand how the individual crystals behave when the aggregate is deformed. Obtaining this information experimentally is difficult, but an idealization can be garnered using the finite element method to model a specific crystal aggregate. In the crystal plasticity finite element method (CPFEM) each crystal in the aggregate is represented by one or more finite elements. The evolution of the crystal orientations is then modeled for a given macroscopic deformation (Asaro and Needleman, 1985; Becker, 1991; Kalidindi et al., 1991; Beaudoin et al., 1993; Sarma and Dawson, 1996). Since the crystal interactions are explicitly modeled, the CPFEM can be utilized to map $\mathbf{L}$ to $\mathbf{L}^c$.

In Engler (2002) and Ma et al. (2004), CPFEM results motivate the application of stochastic variations of $\mathbf{L}$ to obtain $\mathbf{L}^c$. Indeed, Sarma and Dawson (1996) found that the components of the crystal strain rates $\mathbf{D}^c = \frac{1}{2}(\mathbf{L}^c + \mathbf{L}^{c\mathrm{T}})$ predicted by the CPFEM follow a normal distribution with mean approximately equal to their aggregate macro-scale counterpart, i.e. $\boldsymbol{\mu}_{\mathbf{D}^c} = \mathbf{D}$. Using this information, Engler (2002) presents the stochastic GIA (SGIA) model in which the $\mathbf{D}^c$ obtained from the GIA model are randomly perturbed according to a normal distribution, resulting in more accurate results. Ma et al. (2004)

modify the FCM so that the $\mathbf{D}^c$ are selected from a normal distribution with mean equal to $\mathbf{D}$. This model appears to give more accurate texture predictions than the FCM with little increase in computational cost. One weakness of these stochastic methods is that they are based on limited CPFEM results that may not illustrate general polycrystal behavior. Another criticism is that they are somewhat empirical and not based on micromechanical principles (Van Houtte et al., 2005). Tonks et al. (2008) validate the model from Ma et al. (2004) using a kinematically determined planar polycrystal, but further validation is needed for three-dimensional (3-D) polycrystals.

The purpose of this work is to examine the validity of using 3-D stochastic variations to obtain $\mathbf{L}^c$ from $\mathbf{L}$ and to compare the performance of such methods to deterministic methods. We begin in Section 2 by extending the CPFEM investigation conducted by Sarma and Dawson (1996). We find that the $\mathbf{L}^c$ distribution in an idealized tantalum polycrystal is approximately normal with mean $\boldsymbol{\mu}_{\mathbf{L}^c} = \mathbf{L}$. We also find that the CPFEM simulations predict that the $\mathrm{tr}(\mathbf{D}^c) \approx \mathrm{tr}(\mathbf{D})$. In Section 3, we draw on these findings to formulate two stochastic methods, the STM, which is based on the method form Ma et al. (2004), and the stochastic no-constraints model (SNCM). In these methods the $\mathbf{L}^c = \mathbf{D}^{c\prime} + \frac{1}{3}\mathrm{tr}(\mathbf{D})\mathbf{I} + \mathbf{W}$ in every crystal, where $\mathbf{W} = \frac{1}{2}(\mathbf{L} - \mathbf{L}^{\mathrm{T}})$ is the skew-symmetric component of $\mathbf{L}$ and $\mathbf{D}^{c\prime} = \mathbf{D}^c - \frac{1}{3}\mathrm{tr}(\mathbf{D}^c)\mathbf{I}$ is the deviatoric component of $\mathbf{D}^c$. The latter are sampled from tensor normal distributions in a Monte Carlo fashion. In both methods the crystal tensor normal distributions are defined by second-order mean tensors and fourth-order covariance tensors which describe the statistical first- and second-moments. The methods define the covariance tensors similarly, but in the STM the mean tensors are equal to $\mathbf{D}'$ while in the SNCM the mean tensors are determined by scaling values of $\mathbf{D}^{c\prime}$ calculated using the NCM. Effectively, the SNCM is complementary to the

SGIA model (Engler, 2002). Finally, in Section 4 we perform calibration and validation of the STM and SNCM using data from compression experiments of tantalum specimens.

2 CPFEM Analyses

Sarma and Dawson (1996) modeled the plain-strain compression of an idealized copper polycrystal and observed the behavior of $\mathbf{D}^c$. The polycrystal contained 1000 cubic crystals of equal size, which they represented as single elements in a $10 \times 10 \times 10$ grid. Both a random initial texture and a simulated compression initial texture were employed in the simulations. They found that the components of the strain rate $\mathbf{D}^c$ followed a normal distribution with the mean equal to the applied strain rate. They also observed that the crystal orientation influenced the $\mathbf{D}^c$ components corresponding to the $\mathbf{D}$ nonzero macroscopic components. For example, if $D_{12} = \mathbf{e}_1 \cdot (\mathbf{D}\mathbf{e}_2) \neq 0$, then the crystal orientation influenced $D^c_{12} = \mathbf{e}_1 \cdot (\mathbf{D}^c\mathbf{e}_2)$.

We seek to find if the observations of Sarma and Dawson (1996) are more universal. To accomplish this, we use the CPFEM to model the deformation of an idealized tantalum polycrystal with 1000 cubic crystals of equal size in a $10 \times 10 \times 10$ grid. The polycrystal is deformed for 0.001 s with three different applied velocity gradients,

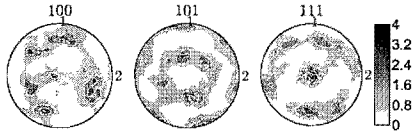

Fig. 1. Pole figures of the tantalum plate initial texture calculated from electron backscatter diffraction data.

$$\mathbf{L}_1 = \begin{bmatrix} 500 & 0 & 200 \\ 0 & 500 & 0 \\ -200 & 0 & -1000 \end{bmatrix} \frac{1}{s}, \mathbf{L}_2 = \begin{bmatrix} 1000 & 200 & 0 \\ -200 & 0 & 0 \\ 0 & 0 & -1000 \end{bmatrix} \frac{1}{s},$$

$$\mathbf{L}_3 = \begin{bmatrix} 0 & 0 & 1000 \\ 0 & 0 & 0 \\ 0 & 0 & 0 \end{bmatrix} \frac{1}{s}, \tag{1}$$

and two different initial textures, a random texture and a texture measured using electron backscatter diffraction from the tantalum plate sample examined in Bronkhorst et al. (2007) (see Fig. 1 for pole figures of the texture). For each loading and initial texture, we observe the behavior of the $\mathbf{L}^c$, separated into the symmetric $\mathbf{D}^c$ and skew-symmetric $\mathbf{W}^c$ components. The analysis is conducted using the CPFEM formulation and implemented via an ABAQUS UMAT as presented in Bronkhorst et al. (2007). In the analysis, we surround the polycrystal with a border of three elements with randomly assigned initial crystal orientations to reduce boundary effects. The nodal displacements on the outer surface of the border elements are prescribed such that the applied velocity gradient is maintained throughout the deformation.

In Section 2.1, we summarize the CPFEM formulation and tantalum material parameters from Bronkhorst et al. (2007). In Section 2.2, we first conduct a convergence study on a reduced polycrystal containing eight crystals to determine the required mesh resolution. We then analyze the full polycrystal to quantify statistics on $\mathbf{D}^c$ and $\mathbf{W}^c$.

2.1 CPFEM Formulation

The historical basis for the CPFEM formulation (Bronkhorst et al., 2007) is found in Rice (1971), Hill and Rice (1972), Kocks et al. (1975), Asaro and Rice (1977), and Asaro (1983b,a), in which thermally activated slip is assumed to be the dominant mechanism for plastic deformation.

A material point in a crystal c identified by position vector $\mathbf{x}^c$ in the reference configuration is mapped to the location in the deformed configuration at time t identified by the position vector $\mathbf{x}_t^c$ through the motion $\mathbf{f}^c$, i.e. $\mathbf{x}_t^c = \mathbf{f}^c(\mathbf{x}^c; t)$. We define the deformation gradient as the spatial derivative, i.e. $\mathbf{F}^c = \nabla \mathbf{f}^c \in \mathrm{Lin}^+$ where Lin^+ is the set of tensors with positive determinant so that the mapping $\mathbf{f}^c$ at a given time t is everywhere invertible.

The material point velocity can be defined with respect to the reference configuration, giving the material velocity, or with respect to the deformed configuration, giving the spatial velocity, i.e.

$$\dot{\mathbf{f}}^c(\mathbf{x}^c; t) = \mathbf{v}^c(\overbrace{\mathbf{x}_t^c}^{\mathbf{f}^c(\mathbf{x}^c;t)}; t). \tag{2}$$

Differentiating this equality with respect to the reference position $\mathbf{x}^c$ and rearranging gives the expression for the spatial crystal velocity gradient

$$\mathbf{L}^c|_{\mathbf{x}_t^c = \mathbf{f}^c(\mathbf{x}^c;t)} = \nabla \mathbf{v}^c|_{\mathbf{x}_t^c = \mathbf{f}^c(\mathbf{x}^c;t)} = \dot{\mathbf{F}}^c\ \mathbf{F}^{c\ -1} \tag{3}$$

The crystal deformation gradient is assumed to be the result of a plastic isochoric deformation $\mathbf{F}_p^c$ followed by an elastic deformation $\mathbf{F}_e^c$, i.e.

$$\mathbf{F}^c = \mathbf{F}_e^c \mathbf{F}_p^c = \mathbf{R}^c \mathbf{U}^c \mathbf{F}_p^c \quad \text{with } \det \mathbf{F}_p^c = 1 \text{ and } \mathbf{R}^c \in \mathrm{Rot} \tag{4}$$

where Rot is the set of all rotations. The plastic deformation $\mathbf{F}_p^c$ is due to shearing along slip planes whereas the elastic deformation $\mathbf{F}_e^c$ is due to elastic stretching of the crystal lattice $\mathbf{U}^c$ and a rigid lattice rotation $\mathbf{R}^c$ which defines the crystal orientation.

We assume the crystal stress results from small elastic strains and thermal expansion due to small temperature changes about the initial temperature θ_0. As such, the second Piola-Kirchhoff stress with respect to the intermediate configuration is calculated from the linear relation

$$\mathbf{T}^{c\star} = \boldsymbol{\mathcal{C}}(\theta^c)\left[\mathbf{E}_e^c - \mathbf{A}(\theta^c - \theta_0)\right], \tag{5}$$

where θ^c is the current crystal temperature, $\boldsymbol{\mathcal{C}}(\theta^c) = \boldsymbol{\mathcal{C}}_0 + \boldsymbol{\mathcal{M}}(\theta^c)$ is the temperature dependent fourth-order crystal elasticity tensor with $\boldsymbol{\mathcal{C}}_0$ the elasticity tensor and $\boldsymbol{\mathcal{M}} = \frac{\mathrm{d}\boldsymbol{\mathcal{C}}}{\mathrm{d}\theta^c}$ at $\theta^c = 0\,\mathrm{K}$, $\mathbf{A} = \alpha \mathbf{I}$ is the second-order isotropic crystal thermal expansion tensor with α the thermal expansion coefficient, and $\mathbf{E}_e^c$ is the Green elastic strain tensor defined as

$$\mathbf{E}_e^c \equiv \frac{1}{2}\left(\mathbf{F}_e^{cT}\mathbf{F}_e^c - \mathbf{I}\right). \tag{6}$$

The second Piola-Kirchhoff stress $\mathbf{T}^{c\star}$ is defined in terms of the Cauchy stress

$\mathbf{T}^c$ as

$$\mathbf{T}^{c\star} \equiv (\det \mathbf{F}_e^c)\mathbf{F}_e^{c-1}\mathbf{T}^c\mathbf{F}_e^{c-\mathrm{T}}. \tag{7}$$

We assume cubic crystal symmetry, such that $\mathcal{C}_0$ and $\mathcal{M}$ are each described by three parameters.

The crystal plastic velocity gradient, defined similarly to Eq. (3), results from the deformation of the crystal lattice along the slip planes as defined by

$$\mathbf{L}_p^c = \sum_{s=1}^{M} \dot{\gamma}^s \, \mathbf{S}_0^s \tag{8}$$

where, for each slip system s, $\dot{\gamma}^s$ is the system shear rate and $\mathbf{S}_0^s = \mathbf{b}_0^s \otimes \mathbf{n}_0^s$ is the Schmidt tensor with $\mathbf{b}_0^s$ and $\mathbf{n}_0^s$ unit vectors in the reference configuration along the slip direction and normal to the slip plane, respectively. We employ two slip modes, the $\{110\}$ slip plane with a $\langle 111 \rangle$ slip direction and the $\{112\}$ plane with the $\langle 111 \rangle$ direction, giving a total of $M = 24$ slip systems in the BCC tantalum.

The slip system shear rate $\dot{\gamma}^s$ is defined using a temperature dependent flow rule (Busso and McClintock, 1996)

$$\dot{\gamma}^s = \dot{\gamma}_0 \exp\left[-\frac{F_0}{k\theta^c}\left\langle 1 - \left\langle \frac{|\tau^s| - \tau_0^s \frac{\mu}{\mu_0}}{\tau_l \frac{\mu}{\mu_0}} \right\rangle^p \right\rangle^q\right] \operatorname{sign}(\tau^s), \tag{9}$$

where τ^s is the slip system resolved shear stress

$$\tau^s = \left(\mathbf{R}^c \mathbf{m}_0^s \, \mathbf{R}^{cT}\right) \cdot \mathbf{T}^{c\prime} \tag{10}$$

with $\mathbf{m}_0^s$ the symmetric component of the Schmidt tensor $\mathbf{S}_0^s$ and the inner product between two tensors $\mathbf{A}$ and $\mathbf{B}$ defined as $\mathbf{A} \cdot \mathbf{B} = \mathrm{tr}(\mathbf{A}\mathbf{B}^{\mathrm{T}})$. Note that the prime denotes the deviatoric component, i.e. $\mathbf{T}^{c\prime} = \mathbf{T}^c - \frac{1}{3}\mathrm{tr}(\mathbf{T}^c)\mathbf{I}$ is the deviatoric Cauchy stress. As seen above, slip resistance results from the dislocation density, represented by the slip system flow stress τ_0^s, and the constant intrinsic lattice resistance τ_l. Both of these quantities are defined at 0 K and the temperature sensitivity is represented to first order through the current crystal temperature θ^c and the shear modulus ratio

$$\frac{\mu}{\mu_0} \approx 1 + \frac{\mathcal{M}_{1212}}{\mathcal{C}_{1212_0}}\theta^c \tag{11}$$

where $\mathcal{C}_{1212_0} = (\mathbf{e}_1 \otimes \mathbf{e}_2) \cdot \mathcal{C}_0[\mathbf{e}_1 \otimes \mathbf{e}_2]$ and $\mathcal{M}_{1212} = (\mathbf{e} \otimes \mathbf{e}_2) \cdot \mathcal{M}[\mathbf{e}_1 \otimes \mathbf{e}_2]$. The model constants are the pre-exponential constant $\dot{\gamma}_0$, the total free energy required to overcome the lattice resistance F_0, the Boltzmann constant k, and the exponential constants q and p. The brackets $\langle x \rangle$ indicate the Heavy side step function, i.e. $\langle x \rangle = x$ for $x > 0$ and $\langle x \rangle = 0$ for $x \leq 0$.

This model accounts for the change in the dislocation density by evolving the flow stress τ_0^s according to

$$\dot{\tau}_0^s = \sum_\beta h_{s\beta} \left|\dot{\gamma}^\beta\right|, \tag{12}$$

where the total hardening rate $h_{s\beta}$ takes the form

$$h_{s\beta} = [r + (1 - r)\delta_{s\beta}]\, h_\beta, \tag{13}$$

which accounts for forest and self-hardening, with r the latent hardening parameter and $\delta_{s\beta}$ the Kronecker delta. The self-hardening rate h_β, resulting from

dislocation generation and annihilation, is defined by Acharya and Beaudoin (2000) as

$$h_\beta = h_0 \left(\frac{s_s^\beta - \tau_0^\beta}{s_s^\beta - \tau_{0_0}} \right), \tag{14}$$

where h_0 is a constant, τ_{0_0} is the initial flow stress, and the saturation stress parameter s_s^β is a function of temperature and shear rate proposed by Kocks (1976), i.e.

$$s_s^\beta = s_{s_0} \left(\frac{\dot{\gamma}^\beta}{\dot{\gamma}_0} \right)^{\frac{k\theta^c}{A}} \tag{15}$$

with constants s_{s_0}, $\dot{\gamma}_0$, and A.

The crystal temperature θ^c is initially equal to θ_0 and is assumed to evolve through adiabatic heating according to

$$\dot{\theta}^c = \frac{\eta}{\rho c_p} \sum_{s=1}^{N} \tau^s \dot{\gamma}^s, \tag{16}$$

where $\eta \in [0,1]$ is the conversion efficiency factor, ρ is the density, and c_p is the specific heat.

For tantalum, we use the parameter values denoted in Table 1 (Bronkhorst et al., 2007).

Table 1
Single crystal model parameters for tantalum from Bronkhorst et al. (2007)

Parameter	Value	Units	Parameter	Value	Units
C_{1111_0}	268.5	GPa	$\mathcal{M}_{1111}$	-0.0245	GPa/K
C_{1122_0}	159.9	GPa	$\mathcal{M}_{1122}$	-0.0118	GPa/K
C_{1212_0}	87.1	GPa	$\mathcal{M}_{1212}$	-0.0149	GPa/K
$\dot{\gamma}_0$	10^7	$\sec^{-1}$	F_0	2.1×10^{-19}	J
τ_l	0.55	GPa	τ_{0_0}	0.05	GPa
p	0.34		q	1.66	
r	1.4		h_0	0.3	GPa
A	10^{-18}	J	s_{s_0}	0.125	GPa
ρ	16640	$\mathrm{kg/m^3}$	c_p	150	J/kg-K
η	0.95		θ_0	298	K
α	6.5	μm/m-K			

2.2 CPFEM Analysis Results

In this section we present the results of the CPFEM analysis. First, we perform a convergence study to determine the number of elements needed to sufficiently resolve each crystal and then summarize the statistical behavior of $\mathbf{D}^c$ and $\mathbf{W}^c$ predicted by the CPFEM.

To determine the changes in the behavior predicted by the CPFEM due to increasing element resolution, we analyze the deformation of a tantalum polycrystal containing 8 crystals. The crystals are arranged in a $2 \times 2 \times 2$ grid with orientations selected from a random initial texture. We deform the reduced polycrystal for 5.0×10^{-4} s with the applied loading $\mathbf{L}_1$ (cf. Eq. (1)) using the CPFEM formulation summarized in section 2.1. Each crystal is resolved evenly by increasing numbers of elements to $1, 8, \ldots, 512$, and changes in the behavior of $\mathbf{L}^c$ and the crystal rotation $\mathbf{R}^c$ are observed. These changes are

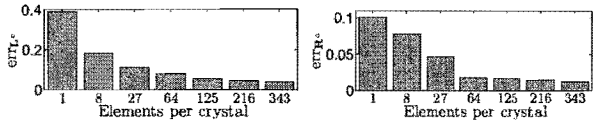

(a) $\mathbf{L}^c$ convergence (b) $\mathbf{R}^c$ convergence

Fig. 2. Changes in the $\mathbf{L}^c$ and $\mathbf{R}^c$ due to increasing element resolution in the CPFEM simulations quantified using Eqs. (17) and (18), respectively. The values are calculated between the element resolution shown in the figure and one resolution finer.

quantified with the error functions

$$\mathrm{err}_{\mathbf{L}^c} = \mathrm{ave}\left(\frac{1}{8}\sum_{c=1}^{8}\frac{\|\mathbf{L}_F^c(t) - \mathbf{L}_C^c(t)\|}{\|\mathbf{L}_F^c(t)\|}\right) \tag{17}$$

$$\mathrm{err}_{\mathbf{R}^c} = \mathrm{ave}\left(\frac{1}{8\pi}\sum_{c=1}^{8}\omega(\mathbf{R}_F^c(t), \mathbf{R}_C^c(t))\right) \tag{18}$$

where the subscripts C and F denote the coarser and finer element resolutions, respectively, $\|\mathbf{L}_F^c(t)\| = \sqrt{\mathrm{tr}(\mathbf{L}_F^{c\mathrm{T}}(t)\,\mathbf{L}_F^c(t))}$ is the norm of $\mathbf{L}_F^c$ at time t, and ω is the angular distance

$$\omega(\mathbf{R}_F^c(t), \mathbf{R}_C^c(t)) = \cos^{-1}\left(\frac{1}{2}\mathrm{tr}\left(\mathbf{R}_F^c(t)\,\mathbf{R}_C^{c\mathrm{T}}(t)\right) - 1\right), \tag{19}$$

which quantifies the difference between the rotations $\mathbf{R}_F^c(t)$ and $\mathbf{R}_C^c(t)$ in radians (Lücke et al., 1986).

Our results show that a further increase in element resolution beyond $7^3 = 343$ elements per crystal results in only small changes in the predicted $\mathbf{L}^c$ and $\mathbf{R}^c$ (see Fig. 2). However, the computational cost of simulating the deformation of the full tantalum polycrystal (1000 crystals) with 343 elements per crystal would be prohibitive. Therefore, we model the polycrystal with $4^3 = 64$ elements per crystal as a compromise between accuracy and computational expense, i.e. the idealized tantalum polycrystal is represented with a $40 \times 40 \times 40$

grid of cubic elements.

The statistical behavior of $\mathbf{D}^c$ and $\mathbf{W}^c$ are observed throughout the deformation of the tantalum polycrystals described previously. Specifically, we observe the shape of the component distributions, the eigenvalues of the $\mathbf{D}^c$ and $\mathbf{W}^c$ covariance tensors, and the influence of the crystal rotation $\mathbf{R}^c$ on $\mathbf{D}^c$ and $\mathbf{W}^c$. We estimate the probability density functions (PDFs) of $\mathbf{D}^c$ and $\mathbf{W}^c$ ($f_{\mathbf{D}^c}$ and $f_{\mathbf{W}^c}$, respectively) using a histogram obtained from the CPFEM results. From the results, it appears that $f_{\mathbf{D}^c}$ and $f_{\mathbf{W}^c}$ follow normal distributions with means equal to the corresponding applied macroscopic values for all three of the applied velocity gradients (cf. Eq. (1)) and both initial textures (see Fig. 3 for results using the $\mathbf{L}_3$ loading and the experimentally obtained plate initial texture). Therefore, $\mathbf{L}^c = \mathbf{D}^c + \mathbf{W}^c$ also follows a normal distribution. Our results are consistent with the findings of Sarma and Dawson (1996) for the uniaxial compression of copper and our results from Tonks et al. (2008) for planar polycrystals. We therefore postulate that $f_{\mathbf{D}^c}$ and $f_{\mathbf{W}^c}$ follow normal distributions for all applied velocity gradients, initial textures, and materials.

These findings raise the question: why do $f_{\mathbf{D}^c}$ and $f_{\mathbf{W}^c}$ tend to follow normal distributions? In CPFEM simulations, the $\mathbf{D}^c$ and $\mathbf{W}^c$ experienced by a specific element depend on the crystal orientation, material parameters, applied boundary conditions, and interactions between neighboring elements/crystals. However, we have found that the shapes of $f_{\mathbf{D}^c}$ and $f_{\mathbf{W}^c}$ are insensitive to the initial texture, material (referencing the results from Sarma and Dawson (1996) and Tonks et al. (2008)), and macroscopic deformation (though the mean and standard deviation of the distributions are not). Therefore, we surmise that the distribution shapes are due primarily to the crystal interactions.

The $\mathbf{D}^c$ and $\mathbf{W}^c$ tensor normal distributions are defined by their second-order

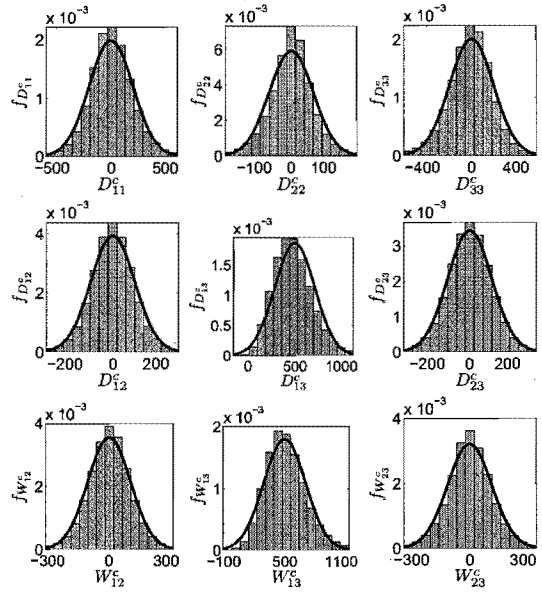

Fig. 3. Histogram approximations (bars) of the terminal $f_{\mathbf{D}^c}$ and $f_{\mathbf{W}^c}$ from the CPFEM results with 64 elements per crystal for the $\mathbf{L}_3$ loading, cf. Eq. (1), and the experimentally obtained plate initial texture. An ideal normal distribution is shown for reference (line). The $f_{\mathbf{D}^c}$ and $f_{\mathbf{W}^c}$ approximately follow normal distributions.

mean tensors and their fourth-order covariance tensors (Basser and Pajevic, 2007). Our CPFEM results have established that the mean tensors $\boldsymbol{\mu}_{\mathbf{D}^c} = \mathbf{D}$ and $\boldsymbol{\mu}_{\mathbf{W}^c} = \mathbf{W}$. Now we use the CPFEM results to investigate the covariance tensors $\boldsymbol{\Sigma}_{\mathbf{D}^c}$ and $\boldsymbol{\Sigma}_{\mathbf{W}^c}$. We calculate $\boldsymbol{\Sigma}_{\mathbf{D}^c}$ and $\boldsymbol{\Sigma}_{\mathbf{W}^c}$ from the CPFEM data as explained in Appendix A and determine the six eigenvalues σ_i^2 of $\boldsymbol{\Sigma}_{\mathbf{D}^c}$ and the three eigenvalues γ_i^2 of $\boldsymbol{\Sigma}_{\mathbf{W}^c}$ (Fig. 4 shows the eigenvalues of $\boldsymbol{\Sigma}_{\mathbf{D}^c}$ and $\boldsymbol{\Sigma}_{\mathbf{W}^c}$ calculated from the CPFEM results). The results show that the eigenvalues are unequal and change with time. In addition, they depend on the macroscopic deformation $\mathbf{L}$ and to a lesser extent on the initial texture. Since

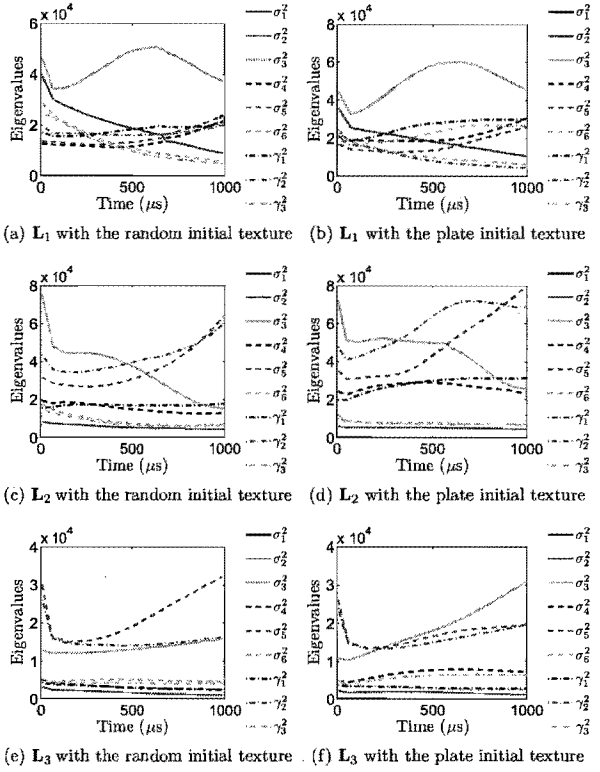

(a) $\mathbf{L}_1$ with the random initial texture (b) $\mathbf{L}_1$ with the plate initial texture

(c) $\mathbf{L}_2$ with the random initial texture (d) $\mathbf{L}_2$ with the plate initial texture

(e) $\mathbf{L}_3$ with the random initial texture (f) $\mathbf{L}_3$ with the plate initial texture

Fig. 4. The eigenvalues of $\boldsymbol{\Sigma}_{\mathbf{D}^c}$ (σ_i^2) and $\boldsymbol{\Sigma}_{\mathbf{W}^c}$ (γ_i^2) over time, calculated from the CPFEM results. See Eq. (1) for the definitions of the $\mathbf{L}_1$, $\mathbf{L}_2$, and $\mathbf{L}_3$ loadings.

the eigenvalues are unequal, $\boldsymbol{\Sigma}_{\mathbf{D}^c}$ is not isotropic and hence depends on the reference frame. The CPFEM results also show that the $\boldsymbol{\Sigma}_{\mathbf{D}^c}$ eigenvalue σ_1^2 is nearly equal to zero, indicating that $\boldsymbol{\Sigma}_{\mathbf{D}^c}$ is rank deficient, with corresponding eigentensor $\boldsymbol{\Phi}_1 \approx \frac{1}{\sqrt{3}}\mathbf{I}$. The covariance tensor is rank deficient because the $\mathbf{D}^c$ in each crystal have approximately the same spherical component $\mathrm{tr}(\mathbf{D}^c) \approx$

$\mathrm{tr}(\mathbf{D})$, e.g. for the $\mathbf{L}_2$ loading and the plate initial texture the aggregate mean $\mu_{\mathrm{tr}(\mathbf{D}^c)} - \mathrm{tr}(\mathbf{D}_2) = -4.1 \times 10^{-3} \|\mathbf{D}_2\|$ and the aggregate standard deviation $\sigma_{\mathrm{tr}(\mathbf{D}^c)} = 1.8 \times 10^{-3} \|\mathbf{D}_2\|$.

To learn if this result occurs with a non-deviatoric applied loading, we conduct an additional CPFEM simulation of the tantalum polycrystal with the random initial texture. The polycrystal is deformed for 5.0×10^{-4} s with the applied velocity gradient

$$\mathbf{L}_4 = \begin{bmatrix} 475 & 0 & 0 \\ 0 & 475 & 0 \\ 0 & 0 & -1000 \end{bmatrix} \frac{1}{s}. \tag{20}$$

Note that the spherical component of $\mathbf{L}$ must be small so as to not violate the small elastic strain assumption. The CPFEM results from the non-deviatoric $\mathbf{L}_4$ loading are consistent with the results from the other loadings. In particular, the predicted $\mathbf{\Sigma}_{\mathbf{D}^c}$ eigenvalue σ_1^2 is nearly equal to zero and $\mathrm{tr}(\mathbf{D}^c) \approx \mathrm{tr}(\mathbf{D})$ in each crystal, i.e. the aggregate mean $\mu_{\mathrm{tr}(\mathbf{D}^c)} - \mathrm{tr}(\mathbf{D}_4) = -4.7 \times 10^{-3} \|\mathbf{D}_4\|$ and the aggregate standard deviation $\sigma_{\mathrm{tr}(\mathbf{D}^c)} = 2.9 \times 10^{-3} \|\mathbf{D}_4\|$.

We postulate that $\mathrm{tr}(\mathbf{D}^c) \approx \mathrm{tr}(\mathbf{D})$ in each crystal due to the effect of the interactions between crystals. Since the elastic strain is small compared to the plastic strain, the crystals interact primarily due to plastic strain. The plastic strain is isochoric and hence the crystal interactions preserve volume. Therefore each crystal experiences the volumetric deformation imposed by the applied strain rate $\mathbf{D}$.

Sarma and Dawson (1996) found that the crystal rotations $\mathbf{R}^c$ primarily influenced the components of $\mathbf{D}^c$ corresponding to the nonzero macroscopic components of $\mathbf{D}$. We further investigate the influence of $\mathbf{R}^c$ on both $f_{\mathbf{D}^c}$ and $f_{\mathbf{W}^c}$ by calculating the number of standard deviations away from the mean, $z_x = (x - \mu_x)/\sigma_x$, that the components of $\mathbf{D}^c$ and $\mathbf{W}^c$ fall for the 1000 crystals in the tantalum polycrystal. We visualize these results with figures similar to inverse pole figures, except that the shading represents values of z_x for a given rotation rather than the pole concentration (see Fig. 5 for the figures calculated at $t = 4\,\mu$s for $z_{D^c_{33}}$, $z_{D^c_{13}}$, and $z_{W^c_{13}}$ using the three loadings with a random initial texture). Our results indicate no significant influence of $\mathbf{R}^c$ on $\mathbf{W}^c$ nor on the components of $\mathbf{D}^c$ for which the corresponding macroscopic components of $\mathbf{D}$ are zero. However, the results do indicate significant influence of $\mathbf{R}^c$ on the components of $\mathbf{D}^c$ corresponding to the nonzero $\mathbf{D}$ components which is consistent with the findings of Sarma and Dawson (1996).

3 Stochastic Polycrystal Plasticity Methods

The CPFEM analyses show that $\mathbf{D}^c$ and $\mathbf{W}^c$ tend to follow normal distributions with $\boldsymbol{\mu}_{\mathbf{D}^c} = \mathbf{D}$ and $\boldsymbol{\mu}_{\mathbf{W}^c} = \mathbf{W}$ due to the crystal interactions. They also show that the $\mathbf{D}^c$ in each crystal have approximately the same spherical component $\mathrm{tr}(\mathbf{D}^c) \approx \mathrm{tr}(\mathbf{D})$. Engler (2002) and Ma et al. (2004) show that varying the $\mathbf{D}^c$ according to a normal distribution in a mean-field polycrystal plasticity model provides an improved description of the polycrystal behavior. We presume that this improvement is because varying the $\mathbf{D}^c$ according to a normal distribution statistically mimics the effects of the crystal interactions. In this section, we build on the work of Engler (2002) and Ma et al. (2004) to develop two methods that approximate the $\mathbf{L}^c$ with stochastic variation,

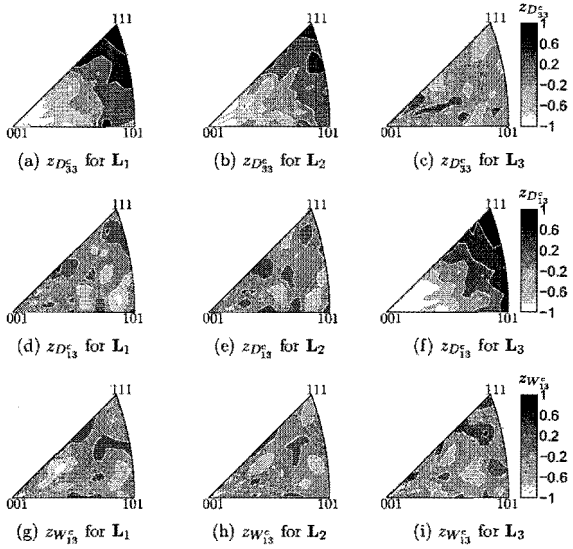

(a) $z_{D^c_{33}}$ for $\mathbf{L}_1$ (b) $z_{D^c_{33}}$ for $\mathbf{L}_2$ (c) $z_{D^c_{33}}$ for $\mathbf{L}_3$

(d) $z_{D^c_{13}}$ for $\mathbf{L}_1$ (e) $z_{D^c_{13}}$ for $\mathbf{L}_2$ (f) $z_{D^c_{13}}$ for $\mathbf{L}_3$

(g) $z_{W^c_{13}}$ for $\mathbf{L}_1$ (h) $z_{W^c_{13}}$ for $\mathbf{L}_2$ (i) $z_{W^c_{13}}$ for $\mathbf{L}_3$

Fig. 5. Inverse pole figures in which the shading represents values of $z_x = (x - \mu_x)/\sigma_x$ for a given rotation rather than the pole concentration. The figures are calculated from the CPFEM results at $t = 4\,\mu$s for $z_{D^c_{33}}$, $z_{D^c_{13}}$, and $z_{W^c_{13}}$ using the three loadings and the random initial texture. See Eq. (1) for the definitions of the $\mathbf{L}_1$, $\mathbf{L}_2$, and $\mathbf{L}_3$ loadings.

the stochastic Taylor model (STM) and the stochastic no-constraints model (SNCM).

For both stochastic methods we treat the deviatoric component of the crystal strain rate $\mathbf{D}^c$ in each crystal as a normally distributed random tensor $\mathbf{D}^{c\prime}$ while the spherical component is equal to the spherical component of $\mathbf{D}$ as indicated by the CPFEM results, i.e.

$$\mathbf{D}^c = \mathbf{D}^{c\prime} + \frac{1}{3}\mathrm{tr}(\mathbf{D})\,\mathbf{I}. \tag{21}$$

However, we assume $\mathbf{W}^c = \mathbf{W}$, though the CPFEM results show that $\mathbf{W}^c$ also follows a normal distribution. This assumption ensures that the PDF of the random tensor is objective and hence material frame invariant (see Appendix B for an objectivity analysis of $\mathbf{L}^c$, $\mathbf{D}^c$, and $\mathbf{W}^c$), and it simplifies the stochastic models. Therefore $\mathbf{L}^c$ is determined from a realization $\mathbb{D}^{c\prime}$ of the random tensor $\mathbf{D}^{c\prime}$, i.e. $\mathbf{L}^c = \mathbb{D}^{c\prime} + \frac{1}{3}\mathrm{tr}(\mathbf{D})\,\mathbf{I} + \mathbf{W}$. The normally distributed PDFs $f_{\mathbf{D}^{c\prime}}$ for the N crystals in the material point aggregate are defined by their second-order mean tensors $\boldsymbol{\mu}_{\mathbf{D}^{c\prime}}$ and their fourth-order covariance tensors $\boldsymbol{\Sigma}_{\mathbf{D}^{c\prime}}$ which quantify the statistical first- and second-moments. The STM and the SNCM differ in their determination of the $\boldsymbol{\mu}_{\mathbf{D}^{c\prime}}$ while their treatment of $\boldsymbol{\Sigma}_{\mathbf{D}^{c\prime}}$ is identical. We emphasize that $\boldsymbol{\mu}_{\mathbf{D}^{c\prime}}$ and $\boldsymbol{\Sigma}_{\mathbf{D}^{c\prime}}$ are the mean and covariance tensors of the random tensor $\mathbf{D}^{c\prime}$ for the specific crystal c while $\boldsymbol{\mu}_{\mathbf{D}^c}$ and $\boldsymbol{\Sigma}_{\mathbf{D}^c}$ are the mean and covariance tensors of $\mathbf{D}^c$ over the entire material point aggregate.

The realization $\mathbb{D}^{c\prime}$ for each crystal is generated in a Monte Carlo fashion according to the distribution $f_{\mathbf{D}^{c\prime}}$. Then, the single crystal model is applied to obtain the crystal Cauchy stress $\mathbf{T}^c$ and evolve the crystal state variables. Once $\mathbf{T}^c$ is calculated for every crystal in the aggregate, the macroscopic polycrystal stress is calculated using a weighted average, i.e.

$$\mathbf{T} = \sum_{c=1}^{N} w_c \mathbf{T}^c, \tag{22}$$

where w_c is the crystal c volume fraction.

In Section 3.1 we summarize the single crystal model used in both stochastic methods. We then describe the distribution of $\mathbf{D}^{c\prime}$ in Section 3.2. Finally, we discuss the details of the STM and SNCM in Sections 3.3 and 3.4, respectively.

3.1 *Single Crystal Model*

Given the current values of state variables (crystal lattice rotation, slip system flow stress, and crystal temperature) and the crystal velocity gradient $\mathbf{L}^c$, the single crystal model determines the crystal Cauchy stress $\mathbf{T}^c$ and evolves the crystal state variables. Note that this model is distinct from that summarized in section 2.1 for the CPFEM and used in Bronkhorst et al. (2007), although it is similar.

We derive the single crystal model starting with the kinematics. As in Eq. (4), the crystal deformation gradient is assumed to be the result of a plastic deformation $\mathbf{F}_p^c$ followed by an elastic deformation $\mathbf{F}_e^c$. Substituting Eq. (4) into Eq. (3), we obtain an expression for the crystal velocity gradient, i.e.

$$\begin{aligned}\mathbf{L}^c &= \left(\dot{\mathbf{R}}^c\mathbf{U}^c\mathbf{F}_p^c + \mathbf{R}^c\dot{\mathbf{U}}^c\mathbf{F}_p^c + \mathbf{R}^c\mathbf{U}^c\dot{\mathbf{F}}^c{}_p\right)\left(\mathbf{F}_p^{c-1}\left(\mathbf{U}^c\right)^{-1}\mathbf{R}^{c\mathrm{T}}\right)\\ &= \dot{\mathbf{R}}^c\mathbf{R}^{c\mathrm{T}} + \mathbf{R}^c\dot{\mathbf{U}}^c\left(\mathbf{U}^c\right)^{-1}\mathbf{R}^{c\mathrm{T}} + \mathbf{R}^c\mathbf{U}^c\mathbf{L}_p^c\mathbf{U}^{c-1}\mathbf{R}^{c\mathrm{T}}. \end{aligned} \tag{23}$$

We assume the elastic strain is small such that $\mathbf{U}_e^c = \mathbf{I} + \boldsymbol{\epsilon}^c$, with $\|\boldsymbol{\epsilon}^c\| \ll 1$. After neglecting terms of $\mathcal{O}(\boldsymbol{\epsilon}^{c2})$,

$$\begin{aligned}\mathbf{L}^c = {}& \dot{\mathbf{R}}^c\mathbf{R}^{c\mathrm{T}} + \mathbf{R}^c\dot{\boldsymbol{\epsilon}}^c\mathbf{R}^{c\mathrm{T}} - \mathbf{R}^c\dot{\boldsymbol{\epsilon}}^c\boldsymbol{\epsilon}^c\mathbf{R}^{c\mathrm{T}} + \mathbf{R}^c\mathbf{L}_p^c\mathbf{R}^{c\mathrm{T}} +\\ & \mathbf{R}^c\boldsymbol{\epsilon}^c\mathbf{L}_p^c\mathbf{R}^{c\mathrm{T}} - \mathbf{R}^c\mathbf{L}_p^c\boldsymbol{\epsilon}^c\mathbf{R}^{c\mathrm{T}}. \end{aligned} \tag{24}$$

The symmetric $\mathbf{D}^c$ and skew-symmetric $\mathbf{W}^c$ components of $\mathbf{L}^c$ are expressed from Eq. (24) as

$$\mathbf{D}^c = \mathbf{R}^c\dot{\boldsymbol{\epsilon}}^c\mathbf{R}^{c\mathrm{T}} + \mathbf{R}^c\mathbf{D}_p^c\mathbf{R}^{c\mathrm{T}} + \mathbf{R}^c\boldsymbol{\epsilon}^c\mathbf{W}_p^c\mathbf{R}^{c\mathrm{T}} - \mathbf{R}^c\mathbf{W}_p^c\boldsymbol{\epsilon}^c\mathbf{R}^{c\mathrm{T}} \tag{25}$$

$$\begin{aligned}\mathbf{W}^c = {}& \dot{\mathbf{R}}^c\mathbf{R}^{c\mathrm{T}} + \mathbf{R}^c\mathbf{W}_p^c\mathbf{R}^{c\mathrm{T}} + \mathbf{R}^c\boldsymbol{\epsilon}^c\mathbf{D}_p^c\mathbf{R}^{c\mathrm{T}} - \mathbf{R}^c\mathbf{D}_p^c\boldsymbol{\epsilon}^c\mathbf{R}^{c\mathrm{T}} -\\ & \frac{1}{2}\mathbf{R}^c\left(\dot{\boldsymbol{\epsilon}}^c\boldsymbol{\epsilon}^c - \boldsymbol{\epsilon}^c\dot{\boldsymbol{\epsilon}}^c\right)\mathbf{R}^{c\mathrm{T}} \end{aligned} \tag{26}$$

where $\mathbf{D}_p^c$ and $\mathbf{W}_p^c$ are the symmetric and skew-symmetric components of $\mathbf{L}_p^c$ and we neglect terms containing $\dot{\boldsymbol{\epsilon}}^c\boldsymbol{\epsilon}^c$ in Eq. (25), since they are small compared to $\dot{\boldsymbol{\epsilon}}^c$.

The deformation of the crystal lattice along the slip planes is defined through $\mathbf{L}_p^c$ by Eq. (8), with $\mathbf{D}_p^c$ and $\mathbf{W}_p^c$ defined by

$$\mathbf{D}_p^c = \sum_{s=1}^{M}\dot{\gamma}^s\mathbf{m}_0^s \tag{27}$$

$$\mathbf{W}_p^c = \sum_{s=1}^{M}\dot{\gamma}^s\mathbf{q}_0^s \tag{28}$$

where $\mathbf{q}_0^s$ is the skew-symmetric component of $\mathbf{S}_0^s$ and the slip system shear rate $\dot{\gamma}^s$ follows from the flow rule in Eq. (9).

We assume that $\mathbf{T}^c$ depends on the elastic component of the deformation gradient and on thermal expansion and that the relationship is isotropic. Note that this is more elastic symmetry than was assumed in the CPFEM formulation from Section 2.1. By linearizing for small elastic strains and assuming no residual stress we obtain

$$\begin{aligned}\mathbf{T}^c = {}& 2\mu(\theta^c)\left(\mathbf{R}^c\boldsymbol{\epsilon}^c\mathbf{R}^{c\mathrm{T}} - \mathbf{R}^c\mathbf{A}(\theta^c - \theta_0)\mathbf{R}^{c\mathrm{T}}\right) +\\ & \lambda(\theta^c)\mathrm{tr}\left(\boldsymbol{\epsilon}^c - \mathbf{A}(\theta^c - \theta_0)\right)\mathbf{I} \end{aligned} \tag{29}$$

$$\mathbf{T}^{c\prime} = 2\mu(\theta^c)\,\mathbf{R}^c\boldsymbol{\epsilon}^{c\prime}\mathbf{R}^{c\mathrm{T}}, \tag{30}$$

where $\mu(\theta^c) = \mu_0 + m_\mu\theta^c$ and $\lambda(\theta^c) = \lambda_0 + m_\lambda\theta^c$ are the temperature dependent Lamé parameters. Substituting Eq. (30) into Eq. (10) gives

$$\begin{aligned}\tau^s &= \tilde{\tau}^s\left(\boldsymbol{\epsilon}^{e\prime},\ \theta^c\right)\\ &= 2\mu(\theta^c)\left(\mathbf{R}^c\mathbf{m}_0^s\,\mathbf{R}^{cT}\right)\cdot\left(\mathbf{R}^c\boldsymbol{\epsilon}^{e\prime}\mathbf{R}^{cT}\right)\\ &= 2\mu(\theta^c)\,\mathbf{m}_0^s\cdot\boldsymbol{\epsilon}^{e\prime}.\end{aligned} \tag{31}$$

As a crystal deforms, the crystal lattice rotates, the dislocation structure evolves, and the temperature increases. These changes are accounted for by evolving the state variables $\mathbf{R}^c$, τ_0^s, and θ^c, respectively. We obtain an expression for the evolution of $\mathbf{R}^c$ by solving Eq. (26) for $\dot{\mathbf{R}}^c$

$$\dot{\mathbf{R}}^c = \mathbf{W}^c\mathbf{R}^c + \mathbf{R}^c\left[-\mathbf{W}_p^c - \boldsymbol{\epsilon}^c\mathbf{D}_p^c + \mathbf{D}_p^c\boldsymbol{\epsilon}^c + \frac{1}{2}(\dot{\boldsymbol{\epsilon}}^c\boldsymbol{\epsilon}^c - \boldsymbol{\epsilon}^c\dot{\boldsymbol{\epsilon}}^c)\right]. \tag{32}$$

An expression for the evolved $\mathbf{R}^c$ is obtained using the fully implicit time integration scheme over the time step Δt of the deviatoric component of Eq. (32) as shown in Kok et al. (2001), i.e.

$$\begin{aligned}\mathbf{R}_t^c = \exp(\mathbf{W}^c\Delta t)\mathbf{R}_{t-\Delta t}^c \exp\Big(\big(&-\mathbf{W}_p^c - \boldsymbol{\epsilon}_t^{c\prime}\mathbf{D}_p^c + \mathbf{D}_p^c\boldsymbol{\epsilon}_t^{e\prime} +\\ &\frac{1}{2}(\dot{\boldsymbol{\epsilon}}^{e\prime}\boldsymbol{\epsilon}_t^{e\prime} - \boldsymbol{\epsilon}_t^{e\prime}\dot{\boldsymbol{\epsilon}}^{e\prime})\big)\Delta t\Big),\end{aligned} \tag{33}$$

where $\mathbf{R}_t^c = \mathbf{R}^c(t)$ and $\dot{\boldsymbol{\epsilon}}_t^{e\prime}$ is approximated by a backward Euler method, i.e. $\dot{\boldsymbol{\epsilon}}_t^{e\prime} \approx \frac{1}{\Delta t}(\boldsymbol{\epsilon}_t^{e\prime} - \boldsymbol{\epsilon}_{t-\Delta t}^{e\prime})$. The evolution of τ_0^s is accounted for by Eq. (12) and the crystal temperature θ^c, initially equal to θ_0, evolves according to Eq. (16). We use the material constants for tantalum from Table 1 with the addition of $\mu_0 = 70.7$ GPa, $m_\mu = -0.0106$ GPa/K, $\lambda_0 = 159.9$ GPa, and $m_\lambda = -0.0118$ Gpa/K.

3.2 *Distribution of* $\mathbf{D}^{e\prime}$

In each crystal we describe the behavior of the random tensor $\mathbf{D}^{e\prime}$ with a tensor normal distribution. Since $\mathbf{D}^{e\prime}$ is a deviatoric symmetric random tensor, we can map it to the 5-dimensional random vector $\mathbf{d}^{e\prime}$ by the five random components

$$\mathrm{d}_i^{e\prime} = \mathbf{V}_i : \mathbf{D}^{e\prime} \text{ for } i = 1, 2, \ldots, 5, \tag{34}$$

where the basis tensors for a deviatoric symmetric tensor $\mathbf{V}_i$ are defined in Appendix A. Inversely, the vector $\mathbf{d}^{e\prime}$ is mapped to the tensor $\mathbf{D}^{e\prime}$ according to

$$\mathbf{D}^{e\prime} = \sum_{i=1}^{5} \mathrm{d}_i^{e\prime}\,\mathbf{V}_i. \tag{35}$$

The first- and second-moments of $\mathbf{d}^{e\prime}$ are defined by the mean vector $\boldsymbol{\mu}_{\mathbf{d}^{e\prime}}$ and the 5×5 covariance matrix $\boldsymbol{\Sigma}_{\mathbf{d}^{e\prime}}$. The first- and second-moments of $\mathbf{D}^{e\prime}$ are defined by the second-order mean tensor $\boldsymbol{\mu}_{\mathbf{D}^{e\prime}}$ and the forth-order covariance tensor $\boldsymbol{\Sigma}_{\mathbf{D}^{e\prime}}$. The mean tensor $\boldsymbol{\mu}_{\mathbf{D}^{e\prime}}$ is obtained from $\boldsymbol{\mu}_{\mathbf{d}^{e\prime}}$ according to the mapping from Eq. (35) and the fourth-order covariance tensor $\boldsymbol{\Sigma}_{\mathbf{D}^{e\prime}}$ is defined in terms of the covariance matrix $\boldsymbol{\Sigma}_{\mathbf{d}^{e\prime}}$ as

$$\boldsymbol{\Sigma}_{\mathbf{D}^{e\prime}} = \sum_{i=1}^{5}\sum_{j=1}^{5} (\boldsymbol{\Sigma}_{\mathbf{d}^{e\prime}})_{ij}\mathbf{V}_i \otimes \mathbf{V}_j. \tag{36}$$

The relationship between a deviatoric symmetric random tensor and the equivalent 5-dimensional vector is described in Appendix A.

Since $\mathbf{D}^{e\prime}$ and $\mathbf{d}^{e\prime}$ are equivalent, their statistical distribution can be equivalently defined in either the vector or tensor form. As described in Appendix

A, the distribution of $\mathbf{D}^{\sigma}$ in each crystal is defined by the mean tensor $\boldsymbol{\mu}_{\mathbf{D}^{\sigma}}$, the covariance tensor $\boldsymbol{\Sigma}_{\mathbf{D}^{\sigma}}$, and the PDF, i.e. the probability that $\mathbf{D}^{\sigma}$ will be a specific realization $\mathbb{D}^{\sigma}$, (Basser and Pajevic, 2007)

$$f_{\mathbf{D}^{\sigma}}(\mathbb{D}^{\sigma}) = \frac{1}{4\pi^2\sqrt{2\pi\ \det \boldsymbol{\Sigma}_{\mathbf{D}^{\sigma}}}} \exp\left(-\frac{1}{2}(\mathbb{D}^{\sigma} - \boldsymbol{\mu}_{\mathbf{D}^{\sigma}}) \cdot \boldsymbol{\Sigma}^{-1}_{\mathbf{D}^{\sigma}}[\mathbb{D}^{\sigma} - \boldsymbol{\mu}_{\mathbf{D}^{\sigma}}]\right) \quad (37)$$

where

$$\det \boldsymbol{\Sigma}_{\mathbf{D}^{\sigma}} = \prod_{i=1}^{5} \sigma_i^2 \quad (38)$$

$$\boldsymbol{\Sigma}^{-1}_{\mathbf{D}^{\sigma}} = \sum_{i=1}^{5} \frac{1}{\sigma_i^2}\, \boldsymbol{\Phi}_i \otimes \boldsymbol{\Phi}_i \quad (39)$$

due to the spectral decomposition

$$\boldsymbol{\Sigma}_{\mathbf{D}^{\sigma}} = \sum_{i=1}^{5} \sigma_i^2\, \boldsymbol{\Phi}_i \otimes \boldsymbol{\Phi}_i, \quad (40)$$

with σ_i^2 the eigenvalues of $\boldsymbol{\Sigma}_{\mathbf{D}^{\sigma}}$ and $\boldsymbol{\Phi}_i$ the corresponding orthonormal eigentensors.

We define $\mathbf{D}^{\sigma}$ in each crystal by assigning $\boldsymbol{\mu}_{\mathbf{D}^{\sigma}}$ and $\boldsymbol{\Sigma}_{\mathbf{D}^{\sigma}}$. The $\boldsymbol{\mu}_{\mathbf{D}^{\sigma}}$ are assigned in different manners in the STM and the SNCM, as described in the following sections. However we assign the $\boldsymbol{\Sigma}_{\mathbf{D}^{\sigma}}$ equally in the two methods. In both methods we define the distributions $f_{\mathbf{D}^{\sigma}}$ in every crystal by the *same* covariance tensor $\boldsymbol{\Sigma}_{\mathbf{D}^{\sigma}}$. As described in Appendix A, $\boldsymbol{\Sigma}_{\mathbf{d}^{\sigma}}$ and hence $\boldsymbol{\Sigma}_{\mathbf{D}^{\sigma}}$ is comprised of 15 independent components due to its symmetry. However assigning 15 components is a daunting task. To investigate if we can reduce the number of independent components, we observe the behavior of the $\mathbf{D}^{c}$ covariance eigenvalues predicted by the CPFEM simulations. Specifically, we

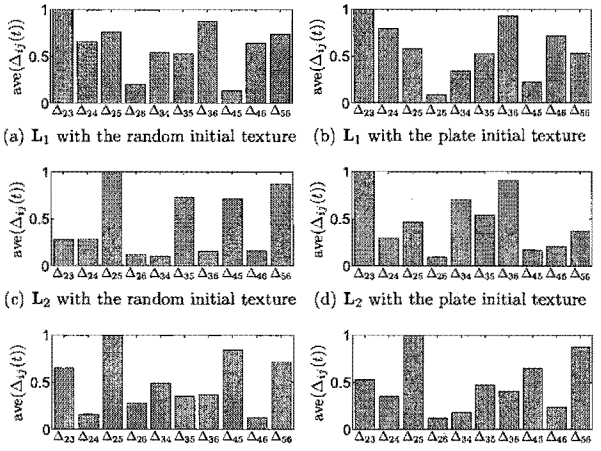

(a) $\mathbf{L}_1$ with the random initial texture (b) $\mathbf{L}_1$ with the plate initial texture

(c) $\mathbf{L}_2$ with the random initial texture (d) $\mathbf{L}_2$ with the plate initial texture

(e) $\mathbf{L}_3$ with the random initial texture (f) $\mathbf{L}_3$ with the plate initial texture

Fig. 6. The time average of the differences $\Delta_{ij} = |\sigma_i^2 - \sigma_j^2|$ between the non-zero eigenvalues of $\mathbf{D}^{c}$ from the CPFEM results, where the values have been normalized such that the largest is equal to one. Note that at least one difference is near zero in each case. See Eq. (1) for the definitions of the $\mathbf{L}_1$, $\mathbf{L}_2$, and $\mathbf{L}_3$ loadings.

calculate the differences between the five non-zero eigenvalues of $\boldsymbol{\Sigma}_{\mathbf{D}^{c}}$ according to $\Delta_{ij}(t) = |\sigma_i^2(t) - \sigma_j^2(t)|$, e.g. $\Delta_{23}(t) = |\sigma_2^2(t) - \sigma_3^2(t)|$. In Fig. 6, we show the time average of the eigenvalues differences, where the average differences have been normalized such that the largest is equal to one. For each loading and initial texture there is at least one difference that is significantly smaller than the others, indicating that the corresponding eigenvalues are nearly equal. By assuming one repeated eigenvalue, we reduce the number of non-zero, distinct eigenvalues to four. Though a repeated eigenvalue does not ensure dependence between components, it does suggest that fewer than 15 components fully define the covariance.

In order to make the assignment of $\boldsymbol{\Sigma}_{\mathbf{D}^{\sigma}}$ feasible, we assume $\boldsymbol{\Sigma}_{\mathbf{D}^{\sigma}}$ is isotropic.

The isotropic covariance tensor of a deviatoric symmetric tensor is defined by a single parameter, i.e.

$$\boldsymbol{\Sigma}_{\mathbb{d}^{c\prime}} = \sigma_n^2 \mathbf{I}_5 \tag{41}$$

where $\mathbf{I}_5$ is the 5×5 identity matrix. By substituting Eq. (41) into Eq. (36) we obtain

$$\boldsymbol{\Sigma}_{\mathbf{D}^{c\prime}} = \sigma_n^2 \boldsymbol{\mathcal{S}} - \frac{1}{3}\sigma_n^2 \mathbf{I} \otimes \mathbf{I} \tag{42}$$

where $\boldsymbol{\mathcal{S}}$ is the fourth-order symmetrizer such that $\boldsymbol{\mathcal{S}}\mathbf{A} = \frac{1}{2}(\mathbf{A} + \mathbf{A}^{\mathrm{T}})$. Therefore $\boldsymbol{\Sigma}_{\mathbf{D}^{c\prime}}$ is completely defined by assigning the single parameter σ_n^2. With $\boldsymbol{\Sigma}_{\mathbb{d}^{c\prime}}$ defined as in Eq. (41), the eigenvalues of $\boldsymbol{\Sigma}_{\mathbf{D}^{c\prime}}$ $\sigma_i^2 = \sigma_n^2$ and the eigentensors $\boldsymbol{\Phi}_i = \mathbf{V}_i$ due to Eqs. (36) and (40). We further simplify the assignment of $\boldsymbol{\Sigma}_{\mathbf{D}^{c\prime}}$ by assuming a constant relationship between σ_n^2 and the norm of the applied strain rate $\|\mathbf{D}\|$.

In our stochastic models, we also use the deviatoric standard normal random symmetric tensor $\mathbf{N}'$ which we describe with the 5-dimensional random vector $\mathbf{n}'$ according to Eq. (34). The random vector $\mathbf{n}'$ has the mean vector $\boldsymbol{\mu}_{\mathbf{n}'} = \mathbf{0}$, the covariance matrix $\boldsymbol{\Sigma}_{\mathbf{n}'} = \mathbf{I}_5$, and the PDF

$$f_{\mathbf{n}'}(\mathbb{n}^{c\prime}) = \frac{1}{2\pi^2\sqrt{2\pi}} \exp\left(-\frac{1}{2}\mathbb{n}^{c\prime} \cdot \mathbb{n}^{c\prime}\right). \tag{43}$$

A realization $\mathbb{n}^{c\prime}$ of the random vector $\mathbf{n}'$ is transformed into the realization $\mathbb{d}^{c\prime}$ of the random vector $\mathbf{d}^{c\prime}$ through the expression

$$\mathbb{d}^{c\prime} = \boldsymbol{\Sigma}_{\mathbf{d}^{c\prime}}^{\frac{1}{2}} \mathbb{n}^{c\prime} + \boldsymbol{\mu}_{\mathbf{d}^{c\prime}}. \tag{44}$$

For the isotropic $\boldsymbol{\Sigma}_{\mathbf{D}^{c\prime}}$ defined in Eq. (41) $\boldsymbol{\Sigma}_{\mathbf{d}^{c\prime}}^{\frac{1}{2}} = \sigma_n \mathbf{I}$. Of course, $\mathbb{d}^{c\prime}$ defines the random tensor realization $\mathbb{D}^{c\prime}$ through Eq. (35).

3.3 Stochastic Taylor Model (STM)

In the STM, each distribution $f_{\mathbf{D}^{c\prime}}$ is defined by the *same* mean tensor $\boldsymbol{\mu}_{\mathbf{D}^{c\prime}} = \mathbf{D}'$ and covariance tensor $\boldsymbol{\Sigma}_{\mathbf{D}^{c\prime}}$. Since $\boldsymbol{\mu}_{\mathbf{D}^{c\prime}} = \mathbf{D}'$ and $\boldsymbol{\Sigma}_{\mathbf{D}^{c\prime}}$ are known without additional computation, the STM generates the realization $\mathbb{D}^{c\prime}$ for each crystal with very little expense. However, we note that $\mathbb{D}^{c\prime}$ and hence $\mathbf{D}^c$ is independent of the crystal rotation $\mathbf{R}^c$, in contrast to the $\mathbf{D}^c$ behavior predicted by the CPFEM (cf. Fig 5).

We obtain a realization $\mathbb{D}^{c\prime}$ for each crystal from a realization $\mathbb{d}^{c\prime}$ with the mapping from Eq. (35). However, $\mathbb{d}^{c\prime}$ is not generated randomly at each time instant t without regard to its history. Rather, it is calculated from a realization $\mathbb{n}^{c\prime}$ of the standard normal random vector $\mathbf{n}'$ that is generated at time $t = 0$, i.e.

$$\mathbb{d}^{c\prime}(t) = \sigma_n \mathbb{n}^{c\prime} + \mathbf{d}'(t) \tag{45}$$

cf. Eqs. (43) and (44), where the vector $\mathbf{d}'(t)$ is obtained from $\mathbf{D}'(t)$ with the mapping from Eq. (34). As seen in Eq. (45), the random perturbation $\mathbb{n}^{c\prime}$ is constant, though $\mathbb{d}^{c\prime}(t)$ will change with time as $\mathbf{d}'(t)$ varies.

After obtaining the realization $\mathbb{D}^{c\prime}(t)$, the crystal velocity gradient is determined according to $\mathbf{L}^c(t) = \mathbb{D}^{c\prime}(t) + \frac{1}{3}\mathrm{tr}(\mathbf{D}(t))\,\mathbf{I} + \mathbf{W}(t)$. Then the single crystal model is used to calculate the Cauchy stress $\mathbf{T}^c(t)$ and evolve the state variables. To evaluate the deviatoric component of the small elastic strain $\boldsymbol{\epsilon}_t^{c\prime}$,

Eqs. (25), (27), (28), and the identity $(\mathbf{A}\,\mathbf{B} - \mathbf{B}\,\mathbf{A})' = \mathbf{A}'\mathbf{B}' - \mathbf{B}'\mathbf{A}'$ are used to obtain the discretized residual equation

$$\mathcal{R}^c(\epsilon_t^{c\prime}) = -\mathbf{R}^{c\mathrm{T}}\mathbb{D}_t^{c\prime}\mathbf{R}^c + \frac{1}{\Delta t}(\epsilon_t^{c\prime} - \epsilon_{t-\Delta t}^{c\prime}) + \sum_{s=1}^{M}\dot{\gamma}^s\left(\mathbf{m}_0^s + \epsilon_t^{c\prime}\mathbf{q}_0^s - \mathbf{q}_0^s\epsilon_t^{c\prime}\right) = \mathbf{0}. \tag{46}$$

We solve the above for $\epsilon_t^{c\prime}$ via a Newton-Raphson iteration, where the Jacobian $\frac{\partial \mathcal{R}^c}{\partial \epsilon_t^{c\prime}}$ is calculated analytically. After solving for $\epsilon_t^{c\prime}$, ϵ_t^c is calculated from

$$\epsilon_t^c = \epsilon_t^{c\prime} + \frac{1}{3}\mathrm{tr}(\epsilon_t^c)\mathbf{I} \;=\; \epsilon_t^{c\prime} + \frac{1}{3}\mathrm{tr}\left(\int_{t-\Delta t}^{t}\dot{\epsilon}^c\,\mathrm{d}t\right)\mathbf{I}$$
$$\approx \epsilon_t^{c\prime} + \frac{1}{3}\left(\mathrm{tr}(\epsilon_{t-\Delta t}^c) + \mathrm{tr}(\mathbf{D}_t)\Delta t\right)\mathbf{I}, \tag{47}$$

where we use the relationship $\mathrm{tr}(\dot{\epsilon}^c) = \mathrm{tr}(\mathbf{D}_t)$ which follows from Eqs. (21) and (25). With ϵ_t^c, the crystal Cauchy stress is calculated from Eq. (29) and the state variables are evolved with Eqs. (12), (16), and (33). Once the $\mathbf{T}^c(t)$ are calculated for each of the N crystals in the material point aggregate, the macroscopic aggregate Cauchy stress $\mathbf{T}(t)$ is calculated from Eq. (22).

As discussed in the previous section, the covariance tensor $\mathbf{\Sigma}_{\mathbf{D}^{c\prime}}$ is defined by the constant parameter σ_n^2 (cf. Eq. (42)). To determine the effect of σ_n^2 on the polycrystal behavior predicted by the STM we conduct STM simulations of the tantalum polycrystal from Section 2. We increase the value of σ_n^2 and observe the resultant changes in the evolving texture. The same N random standard normal vectors $\mathfrak{n}^{c\prime}$ are used in each simulation (cf. Eq. (45)) such that any observed differences in the predicted textures are due to increases in σ_n^2 and not to random variation in the $\mathbb{D}^{c\prime}$. From the results (Fig. 7 shows the change of the texture evolution with σ_n^2 for the $\mathbf{L}_1$ loading and a random initial

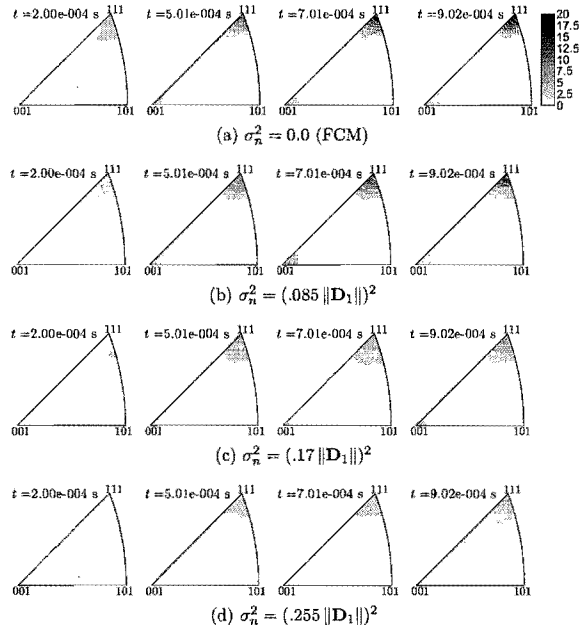

(a) $\sigma_n^2 = 0.0$ (FCM)

(b) $\sigma_n^2 = (.085\,\|\mathbf{D}_1\|)^2$

(c) $\sigma_n^2 = (.17\,\|\mathbf{D}_1\|)^2$

(d) $\sigma_n^2 = (.255\,\|\mathbf{D}_1\|)^2$

Fig. 7. Compression-axis inverse pole figures of the polycrystal texture predicted by the STM at various times t with increasing values of σ_n^2 for the $\mathbf{L}_1$ loading and the random initial texture, suggesting that increases in σ_n^2 slow the rate of texture evolution. The same random standard normal vectors $\mathfrak{n}^{c\prime}$ are used in each simulation.

texture), we conclude that increases in σ_n^2 slow the rate of texture evolution but do not change the relative nature of the evolving texture. This result is similar to the observations from Tonks et al. (2008) for a planar polycrystal.

Since $f_{\mathbf{D}^{c\prime}}$ follows a normal distribution presumably due to the crystal interactions, we assume that the magnitude of those interactions affects the parameter σ_n^2. Indeed, the crystals interact due to their misorientation with neighboring crystals and the anisotropic nature of their elastic and plastic

material response. Therefore, aggregates in which the average misorientation between crystals is small will have few interactions and hence σ_n^2 will be small. Similarly, polycrystals in which the single crystal material response is near isotropic will also have few crystal interactions and a small σ_n^2 value.

The value of σ_n^2 for a specific material and loading are determined by fitting the texture predicted by the STM to that predicted by a CPFEM simulation or measured from experiment. The textures can be represented by either the ODF or pole figures. In Section 4 we determine σ_n^2 by fitting inverse pole figures of the predicted textures to those measured from tantalum compression experiments.

3.4 Stochastic No-Constraints Model (SNCM)

In the SNCM, every crystal strain rate distribution $f_{\mathbf{D}^{c\prime}}$ is described by the same covariance tensor $\mathbf{\Sigma}_{\mathbf{D}^{c\prime}}$ defined by the constant parameter σ_n^2 (cf. Eq. (42)). However, *each* $f_{\mathbf{D}^{c\prime}}$ is defined by a distinct mean tensor $\boldsymbol{\mu}_{\mathbf{D}^{c\prime}}$. We determine the $\boldsymbol{\mu}_{\mathbf{D}^{c\prime}}$ by scaling crystal strain rates calculated using the NCM, such that the $\boldsymbol{\mu}_{\mathbf{D}^{c\prime}}$ are influenced by the corresponding crystal rotations $\mathbf{R}^c$. To this end, we first summarize the NCM following Chastel and Dawson (1994) and then we describe the SNCM.

The NCM ensures stress equilibrium in the crystals by assuming a homogeneous stress in the aggregate, i.e. $\mathbf{T}^c = \mathbf{T}$. Hence, the NCM maintains equilibrium but sacrifices compatibility. Given an applied velocity gradient $\mathbf{L}$, the NCM solves for the deviatoric strain rate in each crystal $\mathbf{D}^{c\prime}$ and the deviatoric component of the polycrystal Cauchy stress $\mathbf{T}'$. The total of $N+1$ tensors are solved at each instant via a Newton-Raphson iteration. The non-linear system

of tensor equations is defined by the N crystal residual equations (Eq. (46)), where Eq. (30) is used with $\mathbf{T}^{c\prime} = \mathbf{T}'$ to define

$$\boldsymbol{\epsilon}_t^{c\prime}(\mathrm{T}') = \frac{1}{2\mu(\theta_t^c)}\mathbf{R}^{c\mathrm{T}}\mathbf{T}'\mathbf{R}^c, \tag{48}$$

such that the residual Eq. (46) is in terms of both the crystal deviatoric strain rate $\mathbf{D}^{c\prime}$ and the macroscopic deviatoric stress $\mathbf{T}'$ rather than the crystal deviatoric elastic strain $\boldsymbol{\epsilon}_t^{c\prime}$. The final equation needed to close the system is the polycrystal residual equation

$$\boldsymbol{\mathcal{R}}^p(\mathbf{D}^{c\prime}) = -\mathbf{D}' + \sum_{c=1}^{N} w^c \mathbf{D}^{c\prime} = \mathbf{0} \tag{49}$$

which ensures that the weighted average of the $\mathbf{D}^{c\prime}$ equals $\mathbf{D}'$ and hence $\boldsymbol{\mu}_{\mathbf{D}^{c\prime}} = \mathbf{D}'$. The Jacobians $\frac{\partial \boldsymbol{\mathcal{R}}^c}{\partial \mathbf{D}^{c\prime}}$, $\frac{\partial \boldsymbol{\mathcal{R}}^c}{\partial \mathbf{T}'}$, and $\frac{\partial \partial \boldsymbol{\mathcal{R}}^p}{\partial \mathbf{D}^{c\prime}}$ ($\frac{\partial \boldsymbol{\mathcal{R}}^p}{\partial \mathbf{T}'} = \mathbf{0}$), where $c = 1, 2, \ldots, N$, are calculated analytically, and the system is efficiently solved at each material point with a sparse, non-linear solver.

The deviatoric crystal strain rates $\mathbf{D}^{c\prime}$ predicted by the NCM are influenced by the corresponding crystal rotations $\mathbf{R}^c$ but are independent of the $\mathbf{D}^{c\prime}$ from the other crystals in the aggregate. For this reason, the $\mathbf{D}^{c\prime}$ predicted by the NCM describe, to a degree, the influence of $\mathbf{R}^c$ on $\mathbf{D}^{c\prime}$. However, since compatibility is not maintained, the $\mathbf{D}^{c\prime}$ predicted by the NCM vary more than those predicted by our CPFEM simulations.

Unlike the STM, in the SNCM each crystal has a unique value of $\boldsymbol{\mu}_{\mathbf{D}^{c\prime}}$ that is influenced by the crystal orientation $\mathbf{R}^c$. The SNCM $\boldsymbol{\mu}_{\mathbf{D}^{c\prime}}$ are defined from the NCM via the difference $\Delta\mathbf{D}^{c\prime} = \mathbf{D}^{c\prime} - \mathbf{D}'$, where $\mathbf{D}^{c\prime}$ is determined from the NCM. Though $\Delta\mathbf{D}^{c\prime}$ describes the influence, we control the strength of that

influence by scaling $\Delta\mathbf{D}^{c\prime}$ by the parameter α_s, i.e.

$$\boldsymbol{\mu}_{\mathbf{D}^{c\prime}} = \mathbf{D}' + \alpha_s \Delta\mathbf{D}^{c\prime}. \tag{50}$$

where $0 \leq \alpha_s \leq 1$. When $\alpha_s = 0$, $\mathbf{R}^c$ does not influence $\boldsymbol{\mu}_{\mathbf{D}^{c\prime}}$ and the method becomes the STM; when $\alpha_s = 1$, the $\boldsymbol{\mu}_{\mathbf{D}^{c\prime}}$ are equal to the $\mathbf{D}^{c\prime}$ calculated by the NCM.

At each time instant t and material point, the deviatoric crystal strain rates $\mathbf{D}^{c\prime}(t)$, $c = 1, 2, \ldots, N$, are calculated using the NCM with a coupled solution of the N crystal residual equations (cf. Eq. (46)) and the polycrystal residual Eq. (49). The $\mathbf{D}^{c\prime}(t)$ are then used to calculate the $\Delta\mathbf{D}^{c\prime}(t) = \mathbf{D}^{c\prime}(t) - \mathbf{D}'(t)$ and $\boldsymbol{\mu}_{\mathbf{D}^{c\prime}}(t)$ via Eq. (50). A realization $\mathbb{D}^{c\prime}(t)$ is subsequently determined from a realization $\mathbb{d}^{c\prime}(t)$ with the mapping from Eq. (35), where

$$\mathbb{d}^{c\prime}(t) = \sigma_n \mathbb{n}^{c\prime} + \boldsymbol{\mu}_{\mathbb{d}^{c\prime}}(t) \tag{51}$$

cf. Eqs. (43) and (44). In the above, $\boldsymbol{\mu}_{\mathbb{d}^{c\prime}}(t)$ is calculated from $\boldsymbol{\mu}_{\mathbf{D}^{c\prime}}(t)$ with the mapping from Eq. (34) and $\mathbb{n}^{c\prime}$ is generated at time $t = 0$. Finally, we calculate $\mathbf{T}^c(t)$ from $\mathbf{L}^c(t) = \mathbb{D}^{c\prime}(t) + \frac{1}{3}\mathrm{tr}(\mathbf{D}(t))\,\mathbf{I} + \mathbf{W}(t)$ and evolve the crystal c state variables in the same manner as in the STM. Once the $\mathbf{T}^c(t)$ are determined for the N crystals in the aggregate, $\mathbf{T}(t)$ is calculated with Eq. (22).

Summarizing, in the SNCM the distribution $f_{\mathbf{D}^{c\prime}}$ for each crystal is defined by Eq. (37) with $\boldsymbol{\mu}_{\mathbf{D}^{c\prime}}$ calculated according to Eq. (50) and $\boldsymbol{\Sigma}_{\mathbf{D}^{c\prime}}$ defined by σ_n^2 according to Eq. (42). While the distribution mean $\boldsymbol{\mu}_{\mathbf{D}^{c\prime}}$ varies from $\mathbf{D}'$ in each crystal, the weighted average satisfies $\sum_{c=1}^{N} w^c \boldsymbol{\mu}_{\mathbf{D}^{c\prime}} = \mathbf{D}'$. Therefore the realizations $\mathbb{D}^{c\prime}$ generated by the SNCM for every crystal in the aggregate tend to satisfy $\sum_{c=1}^{N} w^c \mathbb{D}^{c\prime} = \mathbf{D}'$, since the realizations are sampled from symmetric

normal distributions.

The $\mathbb{D}^{c\prime}$ generated using the SNCM are influenced by σ_n^2 through $\boldsymbol{\Sigma}_{\mathbf{D}^{c\prime}}$ and α_s through the $\boldsymbol{\mu}_{\mathbf{D}^{c\prime}}$. In the previous section we concluded that increases in σ_n^2 slow the rate of texture evolution but do not change the relative nature of the evolving texture. In order to understand the effect of α_s on the predicted textures, we systematically alter its value while holding σ_n^2 constant and observe the resultant changes in the final texture. Again, we use the same random standard normal vectors $\mathbb{n}^{c\prime}$ in each simulation (cf. Eq. (51)). From the analysis (see Fig. 8 for examples of the final texture predicted by the SNCM for various combinations of loading and initial texture with increasing values of α_s), it appears that increases in α_s change the nature of the evolving texture, e.g. for the $\mathbf{L}_1$ loading (cf. Fig. 8(a)), the strength of the $\langle 001 \rangle$ region in the inverse pole figure increases with increasing α_s while the strength of the $\langle 111 \rangle$ region decreases.

The values of σ_n^2 and α_s are determined by fitting textures predicted by the SNCM to those predicted by the CPFEM or measured from experiment. In section 4 we determine values of σ_n^2 and α_s by fitting inverse pole figures of the predicted textures to those measured from tantalum compression experiments.

Since the realizations $\mathbb{D}^{c\prime}$ generated with the SNCM are influenced by the corresponding rotations $\mathbf{R}^c$, they are more consistent with the findings of our CPFEM analysis then the $\mathbb{D}^{c\prime}$ generated using the STM. However the cost of first calculating values of $\mathbf{D}^{c\prime}$ with the NCM makes the overall computational cost of the SNCM three times more expensive than the STM.

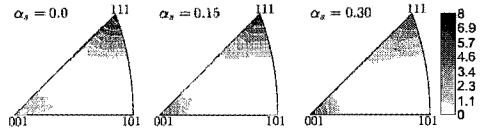

(a) Compression-axis inverse pole figures of the final texture from the $\mathbf{L}_1$ loading and the random initial texture, $\sigma_n^2 = (0.18\|\mathbf{D}_1\|)^2$.

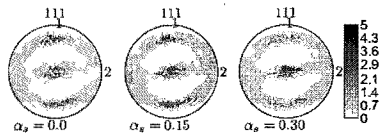

(b) {111} pole figures of the final texture from the $\mathbf{L}_2$ loading and the random initial texture, $\sigma_n^2 = (0.18\|\mathbf{D}_2\|)^2$.

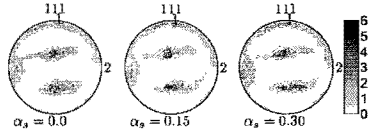

(c) {111} pole figures of the final texture from the $\mathbf{L}_3$ loading and the plate initial texture, $\sigma_n^2 = (0.17\|\mathbf{D}_3\|)^2$.

Fig. 8. Final textures as predicted by the SNCM for increasing values of α_s with various combinations of applied velocity gradient and initial texture, suggesting that increases in α_s change the evolving texture. The same random standard normal vectors $\mathbf{n}^{cr}$ are used in each simulation.

4 Model Calibration and Validation

In this section we calibrate the STM and SNCM by determining values of σ_n^2 and α_s by fitting predicted textures to those measured from tantalum compression experiments. We then validate the models by predicting the textures from different tantalum compression specimens and comparing to the measured textures.

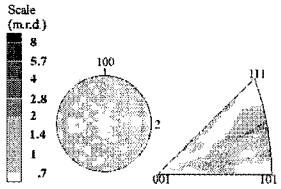

Fig. 9. A {100} pole figure and a compression-axis inverse pole figure of the as-rolled tantalum bar initial texture, calculated from a set of 1000 discrete orientations extracted from x-ray diffraction data.

We employ the upset-forging, i.e. uniaxial compression, experiments from Bingert et al. (1997). In the experimental investigation, cylindrical samples with a diameter of 2.5 cm were compressed at quasi-static strain rates to true axial strains ranging from $\epsilon = -0.5$ to -2.0. Samples were taken from two tantalum sources. Three samples were taken from a powder metallurgy (P/M) blank which exhibits a random initial texture. Two samples were taken from as-rolled bar stock with a preferred texture,[1] where the longitudinal axis coincides with the sample axial direction (see Fig. 9 for a {100} pole figure and a compression-axis inverse pole figure of the measured as-rolled bar texture).

The three P/M samples were compressed to $\epsilon = -0.5, -1.0$, and -2.0, respectively, and the two as-rolled bar samples were compressed to $\epsilon = -1.0$ and -2.0. The five samples were loaded on an MTS load frame at room temperature between metal plates lubricated with MoS_2 grease. The deformed samples were sectioned at various positions, followed by a tantalum-specific metallographic preparation (Kelly et al., 1996). The section textures were measured with x-ray diffraction and pole figures were calculated. In spite of periodic relubrication, surface friction affected the stress state near the surface and center axis of the samples (see Fig. 10). Therefore, we compare the predicted

[1] Note that the as-rolled bar texture is not the same as the plate texture (Fig. 1) used in the previous sections.

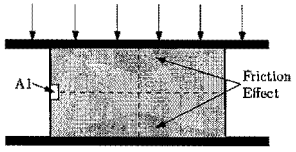

Fig. 10. Schematic of the tantalum upset-forgings. The simulations are compared to the texture measured in the region labeled A1 on the figure.

textures to textures measured from the region in the mid-plane of the sample near the outer radius (labeled as A1 in Fig. 10), where the friction effect is minimized.

The 1000 initial orientations used for the simulations were discretized from the measured initial textures using the method outlined by Kocks et al. (1990). To simplify the analysis, we assume a uniform quasi-static uniaxial compression loading, such that one material point aggregate with $N = 1000$ crystals describes the behavior throughout the region of interest.

We begin in section 4.1 by determining the value of σ_n^2 for the STM and the values of σ_n^2 and α_s for the SNCM by fitting inverse pole figures of the predicted P/M forging textures to inverse pole figures of the measured P/M textures. We then use those parameter values to estimate the textures of the as-rolled bar forgings in Section 4.2.

In both Sections we also estimate the texture in the forgings using the FCM and VPSC to provide benchmarks for the STM and SNCM. The VPSC simulations are conducted with the grain co-rotation scheme in which randomly selected pairs of grains are forced to co-rotate; it has been shown to improve the texture predictions (Li et al., 2005).

4.1 Calibration

During the P/M forging, the experimental data indicates that a nearly equally weighted duplex ⟨001⟩ / ⟨111⟩ texture that is parallel to the compression axis quickly forms (Fig. 11(a)). The ⟨001⟩ and ⟨111⟩ regions in the inverse pole figure sharpen from 8 multiples of a random distribution (m.r.d.) at $\epsilon = -0.5$ to nearly 16 m.r.d. at $\epsilon = -2.0$.

We first predict the P/M forging textures using the STM and determine the value for σ_n^2. By comparing the strengths of the ⟨001⟩ and ⟨111⟩ regions in inverse pole figures of the measured and predicted textures, we find that the value $\sigma_n^2 = (0.16\|\mathbf{D}\|)^2$ provides the most "accurate" fit. With $\sigma_n^2 = (0.16\|\mathbf{D}\|)^2$, the STM predicts the development of the ⟨111⟩ region similar to what was seen in the experiment (Fig. 11(b)). However, it significantly under-predicts the development of the ⟨001⟩ region, predicting a strength of 2 m.r.d. at $\epsilon = -0.5$ and 4 m.r.d. at $\epsilon = -2.0$.

For the SNCM, we determine the values $\sigma_n^2 = (0.16\|\mathbf{D}\|)^2$ and $\alpha_s = 0.2$ by fitting the predicted P/M forging textures to the measured textures. Using the fitted $\sigma_n^2 = (0.16\|\mathbf{D}\|)^2$ and $\alpha_s = 0.2$ values, the SNCM accurately predicts the development of the ⟨111⟩ region (Fig. 11(c)), as did the STM. In addition, the SNCM predicts the strength of the ⟨001⟩ region more accurately than the STM, i.e. the predicted ⟨001⟩ region sharpens from 4 m.r.d. at $\epsilon = -0.5$ to nearly 8 m.r.d. at $\epsilon = -2.0$.

The VPSC model predicts that the ⟨111⟩ region of the P/M forging inverse pole figure sharpens from nearly 4 m.r.d. at $\epsilon = -0.5$ to nearly 16 m.r.d. at $\epsilon = -2.0$ and that the ⟨001⟩ region sharpens from nearly 4 m.r.d. at $\epsilon = -0.5$ to nearly 8 m.r.d. at $\epsilon = -2.0$ (Fig. 11(d)). Therefore the STM predicts

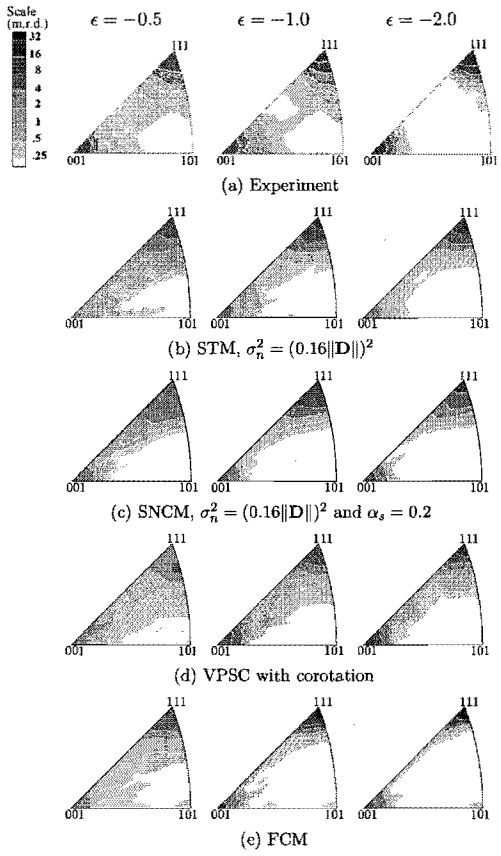

Fig. 11. Compression-axis inverse pole figures of the texture from the P/M upset-forging at three levels of strain from experiment and predicted using various mean-field polycrystal plasticity methods. The σ_n^2 and α^s values for the STM and SNCM are determined by comparing the predicted and measured textures.

the texture development in the P/M forgings less accurately than the VPSC while the SNCM predicts textures similar to those predicted by the VPSC. The FCM drastically over-predicts the development of the ⟨111⟩ region, with the predicted ⟨111⟩ region sharpening from 8 m.r.d. at $\epsilon = -0.5$ to over 32 m.r.d. at $\epsilon = -2.0$, while it under-predicts the development of the ⟨001⟩ region (Fig. 11(e)).

4.2 Validation

We evaluate the accuracy with which the STM and SNCM predict the as-rolled bar forging textures by comparing the strengths of the ⟨001⟩ and ⟨111⟩ regions of the inverse pole figures. We also compare the symmetry of the textures as shown in a {100} pole figure.

The experimental data indicate that a ⟨001⟩/⟨111⟩ duplex texture forms in the as-rolled bar forging, as it does in the P/M forging. The ⟨111⟩ region of the inverse pole figure sharpens from over 4 m.r.d. at $\epsilon = -1.0$ to over 8 m.r.d. at $\epsilon = -2.0$, while the ⟨001⟩ region weakens from nearly 8 m.r.d. at $\epsilon = -1.0$ to 5.7 m.r.d. at $\epsilon = -2.0$ (Fig. 12(a)). Also, the developing texture is not axisymmetric, as exhibited by the {100} pole figure.

All the modeling methods over-predict the strength of the ⟨111⟩ region at $\epsilon = -1.0$ in the as-rolled bar forging and under-predict the strength of the ⟨001⟩ region. They also all predict an axisymmetric texture. The STM predicts the strength of the ⟨111⟩ region at $\epsilon = -2.0$ as over 8 m.r.d., consistent with the experiment (Fig. 12(b)). Similar to the P/M forging, the STM under-predicts the strength of the ⟨001⟩ region, i.e. it predicts a strength of 2.8 m.r.d. The SNCM predicts the strength of the ⟨111⟩ region as over 8 m.r.d. at $\epsilon = -2.0$

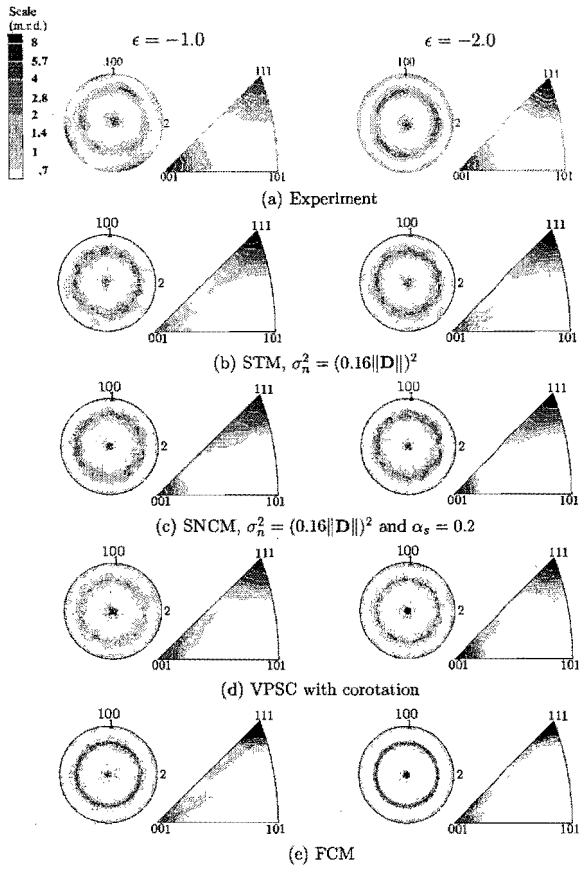

Fig. 12. Compression-axis inverse pole figures and {100} pole figures of the texture from the as-rolled bar upset-forging at two levels of strain from experiment and predicted using various mean-field polycrystal plasticity methods.

and the strength of the ⟨001⟩ region as 5.7 m.r.d., thus accurately predicting the experimental texture (Fig. 12(c)). At $\epsilon = -2.0$ the VPSC predicts the strength of the ⟨111⟩ region as over 8 m.r.d. and the strength of the ⟨001⟩ region as 8 m.r.d. (Fig. 12(d)). As with the P/M forgings, the VPSC predicts the development of the texture in the as-rolled bar forgings more accurately than the STM, but it predicts the development slightly less accurately than the SNCM. The FCM predicts a much stronger ⟨111⟩ region at $\epsilon = -2.0$ than that indicated by the experiment, though it accurately predicts the strength of the ⟨001⟩ region (Fig. 12(e)).

Though the STM predicts the texture development in the upset-forgings less accurately than both the SNCM and the VPSC, it is most noteworthy for its computational efficiency. The FCM is the most efficient model, requiring N solutions of the crystal residual Eq. (46) at each time instant to calculate the macro-scale aggregate stress $\mathbf{T}$, but it significantly over-predicts the texture development in the upset-forgings. The STM is nearly as efficient as the FCM, where the increase in cost is attributed to the modest Monte Carlo generation of the $\mathbb{D}^{\sigma}$, and it predicts the textures much more accurately than the FCM. While the VPSC predicts the texture development in the upset-forgings more accurately than the STM, it is also more expensive because it requires multiple solutions of N crystal residual equations to identify the properties of the average homogeneous medium (Lebensohn and Tomé, 1993). The SNCM is three times more expensive than the STM since it requires an NCM solution, i.e. a solution of N+1 coupled nonlinear Eqs. (46) and (49). However, it predicts upset-forging textures similar to those predicted by the VPSC and is more efficient when the VPSC requires more than three iterations, which is often the case. Due to its accuracy and efficiency, the STM is a valuable method for approximating $\mathbf{L}^c$, though the SNCM or VPSC can be employed

when more accuracy is necessary.

5 Conclusions

We have developed two stochastic methods for obtaining $\mathbf{L}^c$ from $\mathbf{L}$ and shown the accuracy with which they model the texture development in tantalum upset-forgings. Our CPFEM analysis of an idealized tantalum polycrystal showed that $\mathbf{D}^c$ and $\mathbf{W}^c$ approximately follow normal distributions with means equal to their macroscopic counterparts. It also showed that for each crystal $\mathrm{tr}(\mathbf{D}^c) \approx \mathrm{tr}(\mathbf{D})$ and that $\mathbf{R}^c$ influences the components of $\mathbf{D}^c$ corresponding to the nonzero $\mathbf{D}$ components. The STM and SNCM build on these findings by treating each deviatoric crystal strain rate $\mathbf{D}^{c\prime}$ as a normally distributed random tensor $\mathbf{D}^{c\prime}$. A realization $\mathbb{D}^{c\prime}$ of each random tensor is generated in a Monte Carlo fashion such that $\mathbf{L}^c = \mathbb{D}^{c\prime} + \frac{1}{3}\mathrm{tr}(\mathbf{D})\mathbf{I} + \mathbf{W}$. The distributions of $\mathbf{D}^{c\prime}$ for every crystal are defined by second-order mean tensors $\boldsymbol{\mu}_{\mathbf{D}^{c\prime}}$ and fourth-order covariance tensors $\boldsymbol{\Sigma}_{\mathbf{D}^{c\prime}}$ which describe the statistical first- and second-moments. For both methods, $\boldsymbol{\Sigma}_{\mathbf{D}^{c\prime}}$ is defined by the constant parameter σ_n^2 (cf. Eq. (42)) in every crystal. However, in the STM $\boldsymbol{\mu}_{\mathbf{D}^{c\prime}} = \mathbf{D}'$ in every crystal while in the SNCM the $\boldsymbol{\mu}_{\mathbf{D}^{c\prime}}$ are determined from deviatoric crystal strain rates calculated using the NCM that have been scaled by the parameter α_s. The $\mathbb{D}^{c\prime}$ determined from the STM are independent of the $\mathbf{R}^c$, whereas the $\mathbf{R}^c$ do influence the $\mathbb{D}^{c\prime}$ in the SNCM.

Calibration and validation of the STM and SNCM were performed using data from compression experiments of tantalum specimens. The STM was shown to be more accurate than the FCM though somewhat less accurate than the VPSC. The results also showed that the SNCM is more accurate than the

STM and approximately equal in accuracy to the VPSC. The STM is extremely computationally efficient, only slightly more expensive than the FCM, while the SNCM is three times more computationally expensive than the STM.

Acknowledgements: This work was partially supported by the DoD/DOE Joint Munitions Technology Development Program.

Appendix A: Random Tensors

Herein, we give representations for symmetric, skew-symmetric, and deviatoric symmetric random tensors. We also provide the tensor normal distribution of a deviatoric symmetric random tensor. Our description of random symmetric tensors is similar to that found in Basser and Pajevic (2007).

Symmetric Random Tensors

We consider a random symmetric tensor $\mathbf{X}$. The symmetric $\mathbf{X}$ is comprised of the random components $\mathsf{X}_{ij} = \mathbf{e}_i \cdot \mathbf{X}\mathbf{e}_j$ with $\mathsf{X}_{ij} = \mathsf{X}_{ji}$. We map the tensor $\mathbf{X}$ to the 6-dimensional random vector $\mathbf{x}$ defined in $\Re^6$ by the six random components

$$\mathsf{x}_i = \mathbf{E}_i \cdot \mathbf{X} \text{ for } i = 1, 2, \ldots, 6, \tag{52}$$

where

$$\begin{aligned}
\mathbf{E}_1 &= \mathbf{e}_1 \otimes \mathbf{e}_1 \quad \mathbf{E}_4 = \frac{1}{\sqrt{2}}(\mathbf{e}_2 \otimes \mathbf{e}_3 + \mathbf{e}_3 \otimes \mathbf{e}_2) \\
\mathbf{E}_2 &= \mathbf{e}_2 \otimes \mathbf{e}_2 \quad \mathbf{E}_5 = \frac{1}{\sqrt{2}}(\mathbf{e}_1 \otimes \mathbf{e}_3 + \mathbf{e}_3 \otimes \mathbf{e}_1) \\
\mathbf{E}_3 &= \mathbf{e}_3 \otimes \mathbf{e}_3 \quad \mathbf{E}_6 = \frac{1}{\sqrt{2}}(\mathbf{e}_1 \otimes \mathbf{e}_2 + \mathbf{e}_2 \otimes \mathbf{e}_1)
\end{aligned} \tag{53}$$

are the orthonormal basis tensors for a symmetric tensor (Pedersen, 1995). Inversely, the vector $\mathbf{x}$ is mapped to the symmetric tensor $\mathbf{X}$ according to

$$\mathbf{X} = \sum_{i=1}^{6} \mathrm{x}_i \, \mathbf{E}_i. \tag{54}$$

The first- and second-statistical moments of the random vector $\mathbf{x}$ are defined by the mean vector and the 6×6 covariance matrix, i.e.

$$\boldsymbol{\mu}_{\mathbf{x}} = \frac{1}{M} \sum_{m=1}^{M} \mathbf{x}_m \tag{55}$$

$$\boldsymbol{\Sigma}_{\mathbf{x}} = \frac{1}{M} \sum_{m=1}^{M} (\mathbf{x}_m - \boldsymbol{\mu}_{\mathbf{x}}) \otimes (\mathbf{x}_m - \boldsymbol{\mu}_{\mathbf{x}}) \tag{56}$$

where we sum over the M realizations $\mathbf{x}_m$. The first- and second-moments of the random tensor $\mathbf{X}$ are defined by the second-order mean tensor and fourth-order covariance tensor, which are defined in terms of $\boldsymbol{\mu}_{\mathbf{x}}$ and $\boldsymbol{\Sigma}_{\mathbf{x}}$ according to

$$\boldsymbol{\mu}_{\mathbf{X}} = \sum_{i=1}^{6} \mu_{\mathrm{x}_i} \, \mathbf{E}_i \tag{57}$$

$$\boldsymbol{\Sigma}_{\mathbf{X}} = \sum_{i=1}^{6} \sum_{j=1}^{6} \Sigma_{\mathrm{x}ij} \mathbf{E}_i \otimes \mathbf{E}_j. \tag{58}$$

By the spectral decomposition theorem we have

$$\boldsymbol{\Sigma}_{\mathbf{X}} = \sum_{i=1}^{6} \sigma_i^2 \, \boldsymbol{\Phi}_i \otimes \boldsymbol{\Phi}_i \tag{59}$$

where σ_i^2 are the eigenvalues of $\boldsymbol{\Sigma}_{\mathbf{X}}$ and $\boldsymbol{\Phi}_i$ are the corresponding orthonormal eigentensors.

Skew-Symmetric Random Tensors

We consider a random skew-symmetric tensor $\mathbf{Y}$. The skew-symmetric $\mathbf{Y}$ is comprised of the random components $\mathrm{Y}_{ij} = \mathbf{e}_i \cdot \mathbf{Y}\mathbf{e}_j$ with $\mathrm{Y}_{ij} = -\mathrm{Y}_{ji}$. We map the random tensor $\mathbf{Y}$ to the 3-dimensional random vector $\mathbf{y}$ defined in $\Re^3$ by the three random components

$$\mathrm{y}_i = \mathbf{G}_i \cdot \mathbf{Y} \text{ for } i = 1, 2, 3, \tag{60}$$

where

$$\begin{aligned}
\mathbf{G}_1 &= \frac{1}{\sqrt{2}}(\mathbf{e}_2 \otimes \mathbf{e}_3 - \mathbf{e}_3 \otimes \mathbf{e}_2) \\
\mathbf{G}_2 &= \frac{1}{\sqrt{2}}(\mathbf{e}_1 \otimes \mathbf{e}_3 - \mathbf{e}_3 \otimes \mathbf{e}_1) \\
\mathbf{G}_3 &= \frac{1}{\sqrt{2}}(\mathbf{e}_1 \otimes \mathbf{e}_2 - \mathbf{e}_2 \otimes \mathbf{e}_1)
\end{aligned} \tag{61}$$

are the basis tensors for a skew-symmetric tensor. Inversely, the vector $\mathbf{y}$ is mapped to the skew-symmetric tensor $\mathbf{Y}$ according to

$$\mathbf{Y} = \sum_{i=1}^{3} \mathrm{y}_i \, \mathbf{G}_i. \tag{62}$$

The first- and second-statistical moments of the random vector $\mathbf{y}$ are defined

by the mean vector and the 3×3 covariance matrix, i.e.

$$\boldsymbol{\mu}_{\mathbf{y}} = \frac{1}{M} \sum_{m=1}^{M} \mathbf{y}_m \tag{63}$$

$$\boldsymbol{\Sigma}_{\mathbf{y}} = \frac{1}{M} \sum_{m=1}^{M} (\mathbf{y}_m - \boldsymbol{\mu}_{\mathbf{y}}) \otimes (\mathbf{y}_m - \boldsymbol{\mu}_{\mathbf{y}}) \tag{64}$$

where we sum over the M realizations $\mathbf{y}_m$. The first- and second-moments of the random tensor $\mathbf{Y}$ are defined by the second-order mean tensor and fourth-order covariance tensor, which are defined in terms of $\boldsymbol{\mu}_{\mathbf{y}}$ and $\boldsymbol{\Sigma}_{\mathbf{y}}$ according to

$$\boldsymbol{\mu}_{\mathbf{Y}} = \sum_{i=1}^{3} \mu_{\mathbf{y}_i} \mathbf{G}_i \tag{65}$$

$$\boldsymbol{\Sigma}_{\mathbf{Y}} = \sum_{i=1}^{3} \sum_{j=1}^{3} \Sigma_{\mathbf{y}_{ij}} \mathbf{G}_i \otimes \mathbf{G}_j. \tag{66}$$

The covariance tensor $\boldsymbol{\Sigma}_{\mathbf{Y}}$ has three non-zero eigenvalues γ_i^2 with corresponding eigentensors $\boldsymbol{\Omega}_i$.

Deviatoric Symmetric Random Tensors

We consider a random deviatoric symmetric tensor $\mathbf{Z}'$. The tensor $\mathbf{Z}'$ is comprised of the random components $\mathrm{Z}'_{ij} = \mathbf{e}_i \cdot \mathbf{Z}' \mathbf{e}_j$ with $\mathrm{Z}'_{ij} = \mathrm{Z}'_{ji}$ and $\mathrm{tr}(\mathbf{Z}') = 0$. We map the tensor $\mathbf{Z}'$ to the 5-dimensional random vector $\mathbf{z}'$ defined in $\Re^5$ by the five random components

$$\mathrm{z}'_i = \mathbf{V}_i \cdot \mathbf{Z}' \text{ for } i = 1, 2, \ldots, 5, \tag{67}$$

where

$$\begin{aligned}
\mathbf{V}_1 &= \frac{1}{\sqrt{2}}(\mathbf{e}_1 \otimes \mathbf{e}_1 - \mathbf{e}_2 \otimes \mathbf{e}_2) \\
\mathbf{V}_2 &= -\frac{1}{\sqrt{6}}(\mathbf{e}_1 \otimes \mathbf{e}_1 + \mathbf{e}_2 \otimes \mathbf{e}_2) + \sqrt{\frac{2}{3}}\,\mathbf{e}_3 \otimes \mathbf{e}_3 \\
\mathbf{V}_3 &= \frac{1}{\sqrt{2}}(\mathbf{e}_2 \otimes \mathbf{e}_3 + \mathbf{e}_3 \otimes \mathbf{e}_2) \\
\mathbf{V}_4 &= \frac{1}{\sqrt{2}}(\mathbf{e}_1 \otimes \mathbf{e}_3 + \mathbf{e}_3 \otimes \mathbf{e}_1) \\
\mathbf{V}_5 &= \frac{1}{\sqrt{2}}(\mathbf{e}_1 \otimes \mathbf{e}_2 + \mathbf{e}_2 \otimes \mathbf{e}_1)
\end{aligned} \tag{68}$$

are the basis tensors for a deviatoric symmetric tensor. Inversely, the vector $\mathbf{z}'$ is mapped to the tensor $\mathbf{Z}'$ according to

$$\mathbf{Z}' = \sum_{i=1}^{5} \mathrm{z}'_i \mathbf{V}_i. \tag{69}$$

From the mapping in Eq. (67) we can express the five components of $\mathbf{z}'$ in terms of the $\mathbf{Z}'$ components, i.e.

$$\begin{aligned}
\mathrm{z}_1 &= \frac{1}{\sqrt{2}}\mathrm{Z}_{11} - \frac{1}{\sqrt{2}}\mathrm{Z}_{22} \\
\mathrm{z}_2 &= -\frac{1}{\sqrt{6}}\mathrm{Z}_{11} - \frac{1}{\sqrt{6}}\mathrm{Z}_{22} + \sqrt{\frac{2}{3}}\mathrm{Z}_{33} \\
\mathrm{z}_3 &= \sqrt{2}\,\mathrm{Z}_{23} = \sqrt{2}\,\mathrm{Z}_{32} \\
\mathrm{z}_4 &= \sqrt{2}\,\mathrm{Z}_{13} = \sqrt{2}\,\mathrm{Z}_{31} \\
\mathrm{z}_5 &= \sqrt{2}\,\mathrm{Z}_{12} = \sqrt{2}\,\mathrm{Z}_{21}.
\end{aligned} \tag{70}$$

The first- and second-statistical moments of the random vector $\mathbf{z}'$ are defined by the mean vector and the 5×5 covariance matrix, i.e.

$$\boldsymbol{\mu}_{\mathbf{z}'} = \frac{1}{M}\sum_{m=1}^{M} \mathbf{z}'_m \tag{71}$$

$$\boldsymbol{\Sigma}_{\mathbf{z}'} = \frac{1}{M}\sum_{m=1}^{M} (\mathbf{z}'_m - \boldsymbol{\mu}_{\mathbf{z}'}) \otimes (\mathbf{z}'_m - \boldsymbol{\mu}_{\mathbf{z}'}) \tag{72}$$

where we sum over the M realizations $\mathbf{z}'_m$. The first- and second-moments of the random tensor $\mathbf{Z}'$ are defined by the second-order mean tensor and fourth-order covariance tensor, which are defined in terms of $\boldsymbol{\mu}_{\mathbf{z}'}$ and $\boldsymbol{\Sigma}_{\mathbf{z}'}$ according to

$$\boldsymbol{\mu}_{\mathbf{Z}'} = \sum_{i=1}^{5} \mu_{\mathbf{z}'i}\, \mathbf{V}_i \tag{73}$$

$$\boldsymbol{\Sigma}_{\mathbf{Z}'} = \sum_{i=1}^{5}\sum_{j=1}^{5} \Sigma_{\mathbf{z}'ij}\, \mathbf{V}_i \otimes \mathbf{V}_j. \tag{74}$$

Inversely, we determine the components of the covariance matrix $\boldsymbol{\Sigma}_{\mathbf{z}'}$ from the covariance tensor $\boldsymbol{\Sigma}_{\mathbf{Z}'}$ with the expression

$$\Sigma_{\mathbf{z}'ij} = \mathbf{V}_i \cdot \boldsymbol{\Sigma}_{\mathbf{Z}'}[\mathbf{V}_j]. \tag{75}$$

The covariance matrix $\boldsymbol{\Sigma}_{\mathbf{z}'}$ is comprised of 25 components. However it follows from Eq. (72) that $\boldsymbol{\Sigma}_{\mathbf{z}'}$ possesses major symmetry, i.e. since $(\mathbf{z}'_m - \boldsymbol{\mu}_{\mathbf{z}'})_i(\mathbf{z}'_m - \boldsymbol{\mu}_{\mathbf{z}'})_j = (\mathbf{z}'_m - \boldsymbol{\mu}_{\mathbf{z}'})_j(\mathbf{z}'_m - \boldsymbol{\mu}_{\mathbf{z}'})_i$ then $(\boldsymbol{\Sigma}_{\mathbf{z}'})_{ij} = (\boldsymbol{\Sigma}_{\mathbf{z}'})_{ji}$.[2] The symmetries of $\boldsymbol{\Sigma}_{\mathbf{z}'}$ reduce the number of independent components to 15.

If we assume that $\mathbf{Z}'$ follows a tensor normal distribution, we can define the probability density function (PDF) of both $\mathbf{z}'$ and $\mathbf{Z}'$. The random vector $\mathbf{z}'$ follows a multinormal distribution defined by the mean vector $\boldsymbol{\mu}_{\mathbf{z}'}$ and the covariance matrix $\boldsymbol{\Sigma}_{\mathbf{z}'}$. The PDF of $\mathbf{z}'$, i.e. the probability that $\mathbf{z}'$ will be a

[2] The two minor symmetries of $\boldsymbol{\Sigma}_{\mathbf{Z}'}$ can also be used to obtain this major symmetry result.

specific realization $\mathbf{z}'$, is given by

$$f_{\mathbf{z}'}(\mathbf{z}') = \frac{1}{4\pi^2\sqrt{2\pi\,\det\boldsymbol{\Sigma}_{\mathbf{z}'}}} \exp\left(-\frac{1}{2}(\mathbf{z}' - \boldsymbol{\mu}_{\mathbf{z}'}) \cdot \boldsymbol{\Sigma}_{\mathbf{z}'}^{-1}(\mathbf{z}' - \boldsymbol{\mu}_{\mathbf{z}'})\right). \tag{76}$$

The tensor normal distribution of the random tensor $\mathbf{Z}'$ is defined by the mean tensor $\boldsymbol{\mu}_{\mathbf{Z}'}$ and the covariance tensor $\boldsymbol{\Sigma}_{\mathbf{Z}'}$, with the PDF, i.e. the probability that $\mathbf{Z}'$ will equal a specific realization $\mathbb{Z}'$, obtained from (Basser and Pajevic, 2007)

$$f_{\mathbf{Z}'}(\mathbb{Z}') = \frac{1}{4\pi^2\sqrt{2\pi\,\det\boldsymbol{\Sigma}_{\mathbf{Z}'}}} \exp\left(-\frac{1}{2}(\mathbb{Z}' - \boldsymbol{\mu}_{\mathbf{Z}'}) \cdot \boldsymbol{\Sigma}_{\mathbf{Z}'}^{-1}[\mathbb{Z}' - \boldsymbol{\mu}_{\mathbf{Z}'}]\right). \tag{77}$$

The values of the determinant and inverse of $\mathbf{Z}'$ are determined with a spectral decomposition of the covariance tensor $\boldsymbol{\Sigma}_{\mathbf{Z}'}$. Since $\mathbf{Z}'$ is symmetric and deviatoric, by the spectral decomposition theorem we have (Basser and Pajevic, 2007)

$$\boldsymbol{\Sigma}_{\mathbf{Z}'} = \sum_{i=1}^{5} \sigma_i^2\, \boldsymbol{\Phi}_i \otimes \boldsymbol{\Phi}_i \tag{78}$$

where σ_i^2 are the eigenvalues of $\boldsymbol{\Sigma}_{\mathbf{Z}'}$ and $\boldsymbol{\Phi}_i$ are the corresponding orthonormal eigentensors. From Eq. (78), we obtain

$$\det \boldsymbol{\Sigma}_{\mathbf{Z}'} = \prod_{i=1}^{5} \sigma_i^2 \tag{79}$$

$$\boldsymbol{\Sigma}_{\mathbf{Z}'}^{-1} = \sum_{i=1}^{5} \frac{1}{\sigma_i^2}\, \boldsymbol{\Phi}_i \otimes \boldsymbol{\Phi}_i. \tag{80}$$

This result is consistent with the singular multinormal distribution defined in Srivastava and von Rosen (2002).

Appendix B: Objectivity Analysis

Objectivity, often referred to as material invariance, requires that descriptions of physical phenomena remain unchanged under rigid body motion. For example, if we consider a rigid rotation $\mathbf{Q}$, the rotated Cauchy stress $\mathbf{T}^\star$ is defined in terms of the unrotated Cauchy stress $\mathbf{T}$ as $\mathbf{T}^\star = \mathbf{Q}\mathbf{T}\mathbf{Q}^{\mathrm{T}}$. For our stochastic polycrystal models, we require that our second-order random tensor be objective, and therefore that its probability density function (PDF) not change due to rigid motion.

Here, we investigate the objectivity of the crystal velocity gradient $\mathbf{L}^c = \dot{\mathbf{F}}^c\,\mathbf{F}^{c-1}$ and its symmetric $\mathbf{D}^c$ and skew-symmetric $\mathbf{W}^c$ components (Malvern, 1969). We begin by defining the rotated crystal deformation gradient

$$\mathbf{F}^{c\star} = \mathbf{Q}\,\mathbf{F}^c. \tag{81}$$

We develop an expression for the rotated crystal velocity gradient $\mathbf{L}^{c\star}$ in terms of $\mathbf{L}^c$ and the rotation $\mathbf{Q}$ according to

$$\begin{aligned}\mathbf{L}^{c\star} &= \dot{\mathbf{F}}^{c\star}\,\mathbf{F}^{c\star-1}\\ &= \left(\dot{\mathbf{Q}}\mathbf{F}^c + \mathbf{Q}\dot{\mathbf{F}}^c\right)\mathbf{F}^{c-1}\mathbf{Q}^{\mathrm{T}}\\ &= \dot{\mathbf{Q}}\mathbf{Q}^{\mathrm{T}} + \mathbf{Q}\dot{\mathbf{F}}^c\mathbf{F}^{c-1}\mathbf{Q}^{\mathrm{T}}\\ &= \dot{\mathbf{Q}}\mathbf{Q}^{\mathrm{T}} + \mathbf{Q}\mathbf{L}^c\mathbf{Q}^{\mathrm{T}}.\end{aligned} \tag{82}$$

From this result we conclude that $\mathbf{L}^c$ is *not* objective, due to the $\dot{\mathbf{Q}}\mathbf{Q}^{\mathrm{T}}$ term. If we look at the symmetric $\mathbf{D}^{c\star} = \frac{1}{2}(\mathbf{L}^{c\star} + \mathbf{L}^{c\star\mathrm{T}})$ and skew-symmetric $\mathbf{W}^{c\star} = \frac{1}{2}(\mathbf{L}^{c\star} - \mathbf{L}^{c\star\mathrm{T}})$ components we find

$$\mathbf{D}^{c\star} = \mathbf{Q}\mathbf{D}^c\mathbf{Q}^{\mathrm{T}} \tag{83}$$

$$\mathbf{W}^{c\star} = \dot{\mathbf{Q}}\mathbf{Q}^{\mathrm{T}} + \mathbf{Q}\mathbf{W}^c\mathbf{Q}^{\mathrm{T}}, \tag{84}$$

where it can be shown that $\dot{\mathbf{Q}}\mathbf{Q}^{\mathrm{T}}$ is skew-symmetric by taking the time derivative of $\mathbf{Q}\mathbf{Q}^{\mathrm{T}} = \mathbf{I}$, i.e.

$$\begin{aligned}\frac{\mathrm{d}(\mathbf{Q}\mathbf{Q}^{\mathrm{T}})}{\mathrm{d}t} &= \frac{\mathrm{d}\mathbf{I}}{\mathrm{d}t}\\ \dot{\mathbf{Q}}\mathbf{Q}^{\mathrm{T}} + \mathbf{Q}\dot{\mathbf{Q}}^{\mathrm{T}} &= \mathbf{0}\\ \dot{\mathbf{Q}}\mathbf{Q}^{\mathrm{T}} &= -\mathbf{Q}\dot{\mathbf{Q}}^{\mathrm{T}}.\end{aligned} \tag{85}$$

Therefore $\mathbf{D}^c$ *is* objective while $\mathbf{W}^c$ is *not*.

Since $\mathbf{L}^c$ and $\mathbf{W}^c$ are not objective, their first- and second-statistical moments, i.e. their second-order mean tensors and fourth-order covariance tensors, are not objective either. Therefore, if we were to assume that $\mathbf{L}^c$ and $\mathbf{W}^c$ followed tensor normal distributions, their PDFs would not be objective. However, since $\mathbf{D}^c$ is objective, its mean and covariance tensors are also objective. If we define the normally distributed random crystal strain rate tensor $\mathbf{D}^c$, its mean tensor in the rotated frame $\boldsymbol{\mu}_{\mathbf{D}^{c\star}}$ is defined as in Eq. (83). The $\mathbf{D}^c$ covariance tensor in the rotated frame is defined as

$$\begin{aligned}\boldsymbol{\Sigma}_{\mathbf{D}^{c\star}} &= \frac{1}{M}\sum_{m=1}^{M}(\mathbb{D}_m^{c\star} - \boldsymbol{\mu}_{\mathbf{D}^{c\star}}) \otimes (\mathbb{D}_m^{c\star} - \boldsymbol{\mu}_{\mathbf{D}^{c\star}})\\ &= \frac{1}{M}\sum_{m=1}^{M}\left(\mathbf{Q}(\mathbb{D}_m^c - \boldsymbol{\mu}_{\mathbf{D}^c})\mathbf{Q}^{\mathrm{T}}\right) \otimes \left(\mathbf{Q}(\mathbb{D}_m^c - \boldsymbol{\mu}_{\mathbf{D}^c})\mathbf{Q}^{\mathrm{T}}\right)\\ &= \frac{1}{M}\sum_{m=1}^{M}(\boldsymbol{\mathcal{Q}}[\mathbb{D}_m^c - \boldsymbol{\mu}_{\mathbf{D}^c}]) \otimes (\boldsymbol{\mathcal{Q}}[\mathbb{D}_m^c - \boldsymbol{\mu}_{\mathbf{D}^c}])\\ &= \boldsymbol{\mathcal{Q}}\left(\frac{1}{M}\sum_{m=1}^{M}(\mathbb{D}_m^c - \boldsymbol{\mu}_{\mathbf{D}^c}) \otimes (\mathbb{D}_m^c - \boldsymbol{\mu}_{\mathbf{D}^c})\right)\boldsymbol{\mathcal{Q}}^{\mathrm{T}}\\ &= \boldsymbol{\mathcal{Q}}\boldsymbol{\Sigma}_{\mathbf{D}^c}\boldsymbol{\mathcal{Q}}^{\mathrm{T}},\end{aligned} \tag{86}$$

where the orthogonal fourth-order tensor $\mathcal{Q} = \mathbf{Q} \boxtimes \mathbf{Q}$ with the fourth-order tensor product $(\mathbf{A} \boxtimes \mathbf{B})[\mathbf{C}] = \mathbf{A}\mathbf{C}\mathbf{B}^{\mathrm{T}}$, and we use the identity $\mathcal{Q}[\mathbf{A}] \otimes \mathcal{Q}[\mathbf{B}] = \mathcal{Q}(\mathbf{A} \otimes \mathbf{B})\mathcal{Q}^{\mathrm{T}}$. Finally, the $\mathbf{D}^e$ PDF in the rotated frame is

$$
\begin{aligned}
f_{\mathbf{D}^{e*}}(\mathbb{D}^{e*}) &= \frac{1}{\sqrt{32\pi^5 \det \boldsymbol{\Sigma}_{\mathbf{D}^{e*}}}} \exp\left(-\frac{1}{2}(\mathbb{D}^{e*} - \boldsymbol{\mu}_{\mathbf{D}^{e*}}) \cdot \boldsymbol{\Sigma}_{\mathbf{D}^{e*}}^{-1}[\mathbb{D}^{e*} - \boldsymbol{\mu}_{\mathbf{D}^{e*}}]\right) \\
&= \frac{1}{\sqrt{32\pi^5 \det(\mathcal{Q}\boldsymbol{\Sigma}_{\mathbf{D}^e}\mathcal{Q}^{\mathrm{T}})}} \\
&\quad \exp\left(-\frac{1}{2}(\mathcal{Q}[\mathbb{D}^e - \boldsymbol{\mu}_{\mathbf{D}^e}]) \cdot \left(\mathcal{Q}\boldsymbol{\Sigma}_{\mathbf{D}^e}^{-1}\mathcal{Q}^{\mathrm{T}}\right)[\mathcal{Q}[\mathbb{D}^e - \boldsymbol{\mu}_{\mathbf{D}^e}]]\right) \\
&= \frac{1}{\sqrt{32\pi^5 \det \boldsymbol{\Sigma}_{\mathbf{D}^e}}} \exp\left(-\frac{1}{2}(\mathbb{D}^e - \boldsymbol{\mu}_{\mathbf{D}^e}) \cdot \boldsymbol{\Sigma}_{\mathbf{D}^e}^{-1}[\mathbb{D}^e - \boldsymbol{\mu}_{\mathbf{D}^e}]\right) \\
&= f_{\mathbf{D}^e}(\mathbb{D}^e), \qquad (87)
\end{aligned}
$$

since the determinant is objective and $\mathcal{Q}$ is orthogonal. Hence, the $\mathbf{D}^e$ PDF is objective.

References

Acharya, A., Beaudoin, A. J., 2000. Grain-size effect in viscoplastic polycrystals at moderate strains. J. Mech. Phys. Solids 48 (10), 2213–30.

Asaro, R., 1983a. Crystal plasticity. J. Appl. Mech. 50 (4B), 921–34.

Asaro, R., 1983b. Micromechanics of crystals and polycrystals. Adv. Appl. Mech. 23, 1–115.

Asaro, R., Needleman, A., 1985. Texture development and strain hardening in rate dependent polycrystals. Acta Metall. 33, 923–53.

Asaro, R., Rice, J., 1977. Strain localization in ductile single crystals. J. Mech. Phys. Solids 25, 309–38.

Basser, P., Pajevic, S., 2007. Spectral decomposition of a 4th-order covariance tensor: applications to diffusion tensor MRI. Signal Process. 87, 220–36.

Beaudoin, A. J., Mathur, K. K., Dawson, P. R., Johnson, G. C., 1993. Three-dimensional deformation process simulation with explicit use of polycrystal plasticity models. Int. J. Plasticity 9 (7), 833–60.

Becker, R., 1991. Analysis of texture evolution in channel die compression - I. Effects of grain interaction. Acta Metall. Mater. 39 (6), 1211–30.

Bingert, J., Desch, P., Bingert, S., Maudlin, P., Tomé, C., 1997. Texture evolution in upset-forged P/M and wrought tantalum: experimentation and modeling. In: Bose, A., Dowding, R. (Eds.), Proc. of 4th Int. Conf. on Tungsten Refractory Metals and Alloys: Processing, Properties, and Applications. Metal Powder Industries Federation, Princeton, NJ, pp. 169–78.

Bronkhorst, C., Hansen, B., Cerreta, E., Bingert, J., 2007. Modeling the microstructural evolution of metallic polycrystalline materials under localization conditions. J. Mech. Phys. Solids 55 (11), 2351–83.

Busso, E., McClintock, F., 1996. Dislocation mechanics-based crystallographic model of a B2-type intermetallic alloy. Int. J. Plasticity 12 (1), 1–28.

Chastel, Y., Dawson, P., 1994. Equilibrium-based model for anisotropic deformations of polycrystalline materials. Mater. Sci. Forum 157, 1747–51.

Crumbach, M., Pomana, G., Wagner, P., Gottstein, G., 2001. A Taylor type deformation texture model considering grain interaction and material properties. Part I - Fundamentals. In: Gottstein, G., Molodov, D. A. (Eds.), Recrystallization and Grain Growth, Proceedings of the First Joint Conference, Springer, Berlin. pp. 1053–60.

Engler, O., 2002. A new approach to more realistic rolling texture simulation. Adv. Eng. Mat. 4 (4), 181–6.

Harren, S. V., Asaro, R. J., 1989. Nonuniform deformations in polycrystals and aspects of the validity of the Taylor model. J. Mech. Phys. Solids 37 (2), 191–232.

Hill, R., Rice, J., 1972. Constitutive analysis of elastic-plastic crystals at arbitrary strain. J. Mech. Phys. Solids 20, 401–13.

Kalidindi, S., Bronkhorst, C., Anand, L., 1992. Crystallographic texture evolution during bulk deformation processing of FCC metals. J. Mech. Phys. Solids 40, 537–69.

Kalidindi, S. R., Bronkhorst, C. A., Anand, L., 1991. On the accuracy of the Taylor assumption in polycrystalline plasticity. In: Anisotropy and localization of plastic deformation. Elsevier appl sci publ ltd, pp. 139–42.

Kelly, A., Bingert, S., Reiswig, R., 1996. New metallographic preparation techniques for tantalum and tantalum alloys. Microstruct. Sci. 23, 185–95.

Kocks, U., Argon, A., Ashby, M., 1975. Thermodynamics and kinetics of slip. In: Progress in Materials Science. Vol. 19. Pergamon Press, New York.

Kocks, U., Tomé, C., Wenk, H.-R., 1998. Texture and Anisotropy. Cambridge University Press.

Kocks, U. F., 1976. Laws for work-hardening and low-temperature creep. J. Eng. Mats. and Tech. 98, 76–85.

Kocks, U. F., Kallend, J. S., Biondo, A. C., 1990. Accurate representations of general textures by a set of weighted grains. Tech. rep., Los Alamos National Laboratory LA-UR-90-2828, Los Alamos, NM.

Kok, S., Beaudoin, A., Tortorelli, D. A., 2001. Numerical integration of lattice rotation in polycrystal plasticity. Int. J. Numer. Meth. Engng 52, 1487–500.

Lebensohn, R., Tomé, C., 1993. A self-consistent anisotropic approach for the simulation of plastic deformation and texture development of polycrystals: application to zirconium alloys. Acta Metall. Mater. 41, 2611–24.

Li, S., Beyerlein, I., Alexander, D., Vogel, S., 2005. Texture evolution during multi-pass equal channel angular extrusion of copper: neutron diffraction characterization and polycrystal modeling. Acta Mater. 53 (7), 2111–25.

Lücke, K., Pospiech, J., Jura, J., Hirsch, J., 1986. On the presentation of orientation distribution functions by model functions. Z. Metallkunde 77 (2), 312–21.

Ma, A., Roters, F., Raabe, D., 2004. Numerical study of textures and lankford values for FCC polycrystals by use of a modified Taylor model. Comput. Mater. Sci. 29, 353–61.

Malvern, L., 1969. Introduction to the Mechanics of a Continuous Medium. Prentice-Hall.

Pedersen, P., 1995. Simple transformations by proper contracted forms: can we change the usual practice? Comm. Numer. Meth. En. 11 (10), 821–9.

Rice, J., 1971. Inelastic constitutive relations for solids: an internal-variable theory and its application to metal plasticity. J. Mech. Phys. Solids 19, 433–55.

Sarma, G. B., Dawson, P. R., 1996. Effects of interactions among crystals on the inhomogeneous deformations of polycrystals. Acta Mater. 44 (5), 1937–53.

Srivastava, M. S., von Rosen, D., 2002. Regression models with unknown singular covariance matrix. Linear Algebra Appl. 354, 255–73.

Taylor, G., 1938. Plastic strain in metals. J. Inst. Metals 62, 307–24.

Tonks, M., Beaudoin, A., Schilder, F., Tortorelli, D., 2008. Investigation of preferred orientations in planar polycrystals. J. Appl. Mech. 75 (5), 051001.

Van Houtte, P., Li, S., Seefeldt, M., Delannay, L., 2005. Deformation texture prediction: from the Taylor model to the advanced lamel model. Int. J. Plasticity 21, 589–624.